# Stellar population properties of individual massive early-type galaxies at 1.4 < z < 2

I. Lonoce,[1,2]⋆ C. Maraston,[3] D. Thomas [ID],[3] M. Longhetti,[1] T. Parikh [ID],[3] P. Guarnieri [ID][3] and J. Comparat[4]

[1]*INAF-Osservatorio Astronomico di Brera, via Brera 28, I-20121 Milano, Italy*
[2]*Department of Astronomy and Astrophysics, The University of Chicago, 5640 South Ellis Avenue, Chicago, IL 60637, USA*
[3]*Institute of Cosmology and Gravitation, University of Portsmouth, Dennis Sciama Building, Burnaby Road, Portsmouth PO1 3FX, UK*
[4]*Max Planck Institute for Extraterrestrial Physics, Giessenbachstrasse 1, D-85748 Garching, Bayern, Germany*

## ABSTRACT

We analyse publicly available, individual spectra of four massive ($M > 10^{11} \, \mathrm{M_\odot}$) early-type galaxies with redshifts in the range $1.4 \leq z \leq 2$ to determine their stellar content, extending our previous work up to $z \sim 2$. The wide wavelength range of the VLT/X-Shooter spectroscopic data in the UV–Optical–NIR arms along with the availability of spectro-photometry allows us to explore different techniques to obtain the stellar population properties, namely through age/metallicity-sensitive spectral indices, full spectral fitting, and broad-band photometric fitting. Moreover, together with the widely used optical Lick indices, we consider further indices in the UV rest frame, and demonstrate that UV indices significantly help the accuracy of the resulting population parameters. We find galaxy ages ranging from 0.2 to 4 Gyr, where the oldest galaxy is found at the lowest redshift, with an excellent agreement between ages determined via indices, full spectral fitting, or broad-band colours. These ages are in perfect agreement with ages of local galaxies at the same velocity dispersion when we assume pure passive evolution. Total metallicities derived from indices show some scatter (between less than half-solar to very high values, $[Z/H] \sim 0.6$). We speculate on possible mechanisms explaining these values, but given the sample size and low S/N of the spectra no conclusion can be made. Indices in the UV rest frame generally lead to similar conclusions as optical indices. For the oldest galaxy (4 Gyr), we show that its UV indices can only be explained by stellar population models including a UV contribution from old stellar populations, suggesting that old, UV bright populations start to inhabit mature galaxies of a few Gyr of age. This is the highest redshift ($z \sim 1.4$) detection of the UV upturn up to date.

**Key words:** galaxies: elliptical and lenticular, cD – galaxies: high-redshift – galaxies: stellar content.

## 1 INTRODUCTION

The stellar population properties of galaxies, such as age, metallicity, and chemical abundance ratios, are key to disclose their past formation and evolution at each cosmic epoch, from the local Universe up to high redshift. In this work, we focus on early-type galaxies (ETGs). In the local Universe, the stellar population properties of ETGs are a clear function of the galaxy stellar mass, with the more massive objects being older, more metal rich, and enhanced in $\alpha$-elements over Iron ($[\alpha/\text{Fe}] \sim 0.3$, e.g. Thomas et al. 2005, 2010; Clemens et al. 2006; Allanson et al. 2009; Parikh

et al. 2019). At a given stellar mass and/or velocity dispersion, a clear homogeneity among the stellar populations of local ETGs is evident, as revealed by the many observed tight scaling relations like the Fundamental Plane of elliptical galaxies, and the age–mass and metallicity–mass relations (e.g. Trager et al. 2000b; Bernardi et al. 2005; Gallazzi et al. 2006; Cresci, Mannucci & Curti 2018; Martín-Navarro et al. 2018). It is also well known that the existence of such tight relations and the properties of ETGs at the massive end challenge predictions from $\lambda$-cold dark matter hierarchical galaxy formation models, where a more gradual and random galaxy build-up with redshift weakens scaling relations and implies a counter dependence between stellar mass and age/abundance ratios to what is observed (Thomas & Kauffmann 1999; Spolaor et al. 2010).

⋆ E-mail: ilonoce@uchicago.edu

Current instrumentation is now capable of acquiring galaxy spectra at increasingly larger cosmic distances, hence the question can be addressed directly on how galaxy stellar populations evolve over cosmic time.

In particular, the chemical content of stellar systems is directly connected to their formation mechanisms from the primordial gas and to the time-scale on which the star formation has taken place (e.g. Thomas et al. 2005; Spolaor et al. 2008; Thomas et al. 2010; de La Rosa et al. 2011; Lonoce et al. 2015; Segers et al. 2016). Detailed metallicity information coupled with age estimates allows one to distinguish between natural (passive) ageing processes and other evolutionary paths as drivers of the evolution of ETGs.

Stellar population properties, in particular the metallicity, are derived from a detailed spectral analysis with stellar population models as it is done for galaxies in the local Universe (e.g. Gallazzi et al. 2005; Spolaor et al. 2008; Trager & Somerville 2009; Thomas et al. 2010).

Moreover, the younger ages of the high-redshift systems (age <2 Gyr) give the important advantage of reducing the well-known age–metallicity degeneracy (e.g. Worthey 1994), easing the determination of these parameters in spite of the lower signal-to-noise ratios of the data.

The approach may make use of few selected spectral indices sensitive to the abundance of specific elements or of the whole spectrum.

Up to now, few pioneering works have been devoted to either the analysis of spectral indices (e.g. Ziegler et al. 2005; Onodera et al. 2012; Jørgensen & Chiboucas 2013; Gallazzi et al. 2014; Jørgensen et al. 2014; Lonoce et al. 2014) or of the full spectrum (e.g. van de Sande et al. 2013; Mendel et al. 2015; Kriek et al. 2016) of high-$z$ ETGs, gaining with the confirmation of their passive status and with some indications of $\alpha$-elements enhanced populations.

In this work, we use a sample of four galaxies in the redshift range $1.4 < z < 2$ taken in both COSMOS (Cosmological Evolution Survey; McCracken et al. 2010) and UKIDSS-UDS (Ultra Deep Survey; Lawrence et al. 2007; Williams et al. 2009) fields, observed with the VLT/X-Shooter instrument covering a wide spectral range from 3000 to 24 800 Å.

We shall use the classical optical Lick/IDS system (i.e. H $\gamma$, H $\beta$, Mg$_b$, etc.) with models sensitive to chemical abundance ratios (Thomas, Maraston & Johansson 2011), in order to gauge our high-$z$ analysis to the $z = 0$ analysis.

Moreover, and originally with respect to previous work, we also explore spectral indices in the UV region (i.e. Mg I, Mg II, Mg$_{\rm wide}$, BL3096, BL3580, etc.) using high-resolution models (Maraston et al. 2009) as well as models including various options for the UV upturn phenomenon (from C. Maraston as used in Le Cras et al. 2016).

This paper is organized as follows. In Section 2, we introduce the sample of ETGs together with the description of the VLT/X-Shooter spectroscopic data. In Section 3, we present the spectral analysis including the measurements of Lick and UV indices and the results obtained from their comparison with the models. In the same section, we test UV-upturned models with the lowest redshift galaxy of the sample (COSMOS-307881). In Sections 4 and 5, we compare the results obtained from the spectral index analysis with both full spectral fitting and wide photometric fitting. In Section 6, we discuss our results and compare them with local scaling relations, discussing possible implications on the redshift evolution of our galaxies. A summary is then found in Section 7.

Throughout this paper, we assume a standard cosmology with $H_0 = 70$ km s$^{-1}$ Mpc$^{-1}$, $\Omega_{\rm m} = 0.3$, and $\Omega_\Lambda = 0.7$.

## 2 THE GALAXY SAMPLE

The galaxy sample we use is composed of four ETGs with spectroscopic redshift in the range $1.4 < z < 2$, which we selected on the basis of the availability of the X-Shooter spectroscopic data. The X-Shooter instrument provides a wide spectral coverage, from the UV to the near-IR, allowing the modelling of several spectral indices (see Section 2.1). Two galaxies, ID-307881 and ID-7447, lie in the COSMOS field (McCracken et al. 2010), and the other two (identified as UDS-19627 and UDS-29410) have been selected from the UKIDSS-UDS field (Lawrence et al. 2007; Williams et al. 2009).

One of the COSMOS objects (COSMOS-307881) has been already analysed by us in Lonoce et al. (2015) using the same spectrum as here, but we include it again as in this paper we perform a wider model analysis including UV indices and upturn models (see Section 3.4). We shall show that only these upturn models can match the observed indices.

The spectra of the other three targets, COSMOS-7447, UDS-19627, and UDS-29410, have been previously analysed by van de Sande et al. (2013) (and references therein), who performed the measurement of the velocity dispersion exploiting the high resolution of the X-Shooter data, in order to study its evolution to $z \sim 0$. They derive stellar population parameters as well as performing spectral fitting on the binned spectra ($\sim$10 Å) using the FAST code (Kriek et al. 2009). Differently from this work, they used the Bruzual & Charlot (2003) models with an exponentially declining star formation history and a Chabrier (2003) initial mass function (IMF).

In this work, we perform a detailed spectral and spectro-photometric analysis of the galaxy stellar populations, using a novel approach that combines optical and UV indices and considers several options for the origin of the UV flux besides that of ongoing star formation.

These ETGs are all bright ($K < 20$), and according to the analysis of van de Sande et al. (2013) they are all massive ($M > 10^{11}$ M$_\odot$, from spectral fitting with a Chabrier IMF but also confirmed from our photometric analysis performed with a Salpeter IMF; see below) and dense objects ($\sigma > 270$ km s$^{-1}$).

Their morphology, as inferred from available *HST* (*Hubble Space Telescope*) (Szomoru et al. 2010) or UKIDSS-UDS (Lawrence et al. 2007) deep imaging, is smoothly elliptical, as already discussed in Lonoce et al. (2015) and in van de Sande et al. (2013). Information about the sample and the parameters derived from the literature (spectroscopic redshift, stellar mass, effective radius, and velocity dispersion) are listed in Table 1. We refer to van de Sande et al. (2013) and Lonoce et al. (2015) (and references therein) for more details.

### 2.1 Spectroscopic data

The spectroscopic observations used in this work have been carried out with the X-Shooter spectrograph on the VLT. The great advantage of X-Shooter is that it obtains high-resolution spectra on a wide spectral range with a single exposure. In particular, it consists of three arms: UVB, VIS, and NIR, which together cover spectral window from 3000 to 24 800 Å with a mean resolution $R \sim 6500$. van de Sande et al. (2013) and Lonoce et al. (2015) have extensively discussed the X-Shooter data, hence here we just summarize their main characteristics (Table 2).

The observing strategy for all the observations is the standard division in exposure blocks with an alternated ABA'B' dithering

**Table 1.** Information and parameters for the sample galaxies: RA (in h, min, and sec), DEC (in deg, arcmin, and arcsec), $K$-band magnitude (AB system), spectroscopic redshift ($z_{spec}$), effective radius ($R_e$), observed velocity dispersion ($\sigma$), and dynamical mass ($\log\mathcal{M}_{dyn}$) determined with the formula of Cappellari et al. (2006).

| ID | RA | DEC | $K$ (AB) | $z_{spec}$ | $R_e$ (kpc) | $\sigma$ (km s$^{-1}$) | $\log\mathcal{M}_{dyn}$ (M$_\odot$) |
|---|---|---|---|---|---|---|---|
| 19627 | 02:18:17.06 | −5:21:38.83 | 20.19 | 2.036 | 1.32 ± 0.17 | 287 ± 39[b] | 11.14 |
| 7447 | 10:00:06.96 | 02:17:33.77 | 19.64 | 1.800 | 1.75 ± 0.21 | 274 ± 51[b] | 11.21 |
| 29410 | 02:17:51.22 | −5:16:21.84 | 19.36 | 1.456 | 1.83 ± 0.23 | 355 ± 98[b] | 11.45 |
| 307881 | 10:02:35.64 | 02:09:14.36 | 19.44 | 1.426 | 2.68 ± 0.12 | 385 ± 85[a] | 11.65 |

*Notes.* [a]See Lonoce et al. (2015).
[b]See van de Sande et al. (2013).

**Table 2.** Observational details for the four ETGs taken from van de Sande et al. (2013) and Lonoce et al. (2015): observation period, exposure time, slit width, program ID, and S/N per dispersion elements before and after the 4000 Å break rest frame.

| ID | Period | Exposure time | Slit | Program ID | S/N (<4000 Å rest frame) | S/N (>4000 Å rest frame) |
|---|---|---|---|---|---|---|
| 19627 | October, 2009 | 1 h + 3 h | 0″.6 + 0″.9 | 084.A-0303(D) | 4 | 7 |
| 7447 | January 22th, 2010 | 1.8 h | 0″.9 | 084.A-1082(A) | 5 | 6 |
| 29410 | July, 2010 | 1.7 h | 0″.9 | 085.A-0962(A) | 4 | 6 |
| 307881 | February 9th, 2011 | 4.3 h | 0″.9 | 086.A-0088(A) | 4 | 7 |

of the vertical source position in the slit. Close to the sources acquisitions, standard stars have been observed during the same nights.

We performed data reduction using the public ESOREX pipeline (Goldoni et al. 2006) for the first steps of the process, while the main procedure has been carried out with the standard IRAF tools.

In more detail, we relied on the pipeline for the standard calibration process (consisting of correction for bias, dark, flat, etc.), checking the output at every single step. Particular care has been given to the identification of the spectral orders, their straightening, and wavelength calibration, where specific hand-made checks have been applied in order to control the pipeline outputs. Furthermore, in each reduction step where the position of the source was involved, we made use of an ancillary code that identifies the source exact position along the slit with high precision in order to further check the output of the ESOREX tool. Indeed, the faintness of our high-redshift objects makes their identification over the noisy underlying sky very difficult, and it was suggested that the ESOREX tools could fail to perform this identification automatically (F. La Barbera, *private communication*). We found that the source position of ESOREX was correct in all cases.

During these first phases of the pipeline, we proceeded following the 'stare' mode (i.e. considering each frame as an independent observation, in opposition to the 'nodding' mode that pairs subsequent observation frames) in order to obtain at the end a single, order-merged, wavelength-calibrated, bi-dimensional spectrum for each observing block.

We then completed the data reduction by means of IRAF performing the sky subtraction, the mono-dimensional spectrum extraction, and its flux calibration. We found that the sky subtraction was obtained more accurately by means of the IRAF tools combined with the possibility to exploit the A–B observing pattern with respect to the ESOREX pipeline. Mono-dimensional spectra within their effective radius $R_e$ have been extracted (see Table 1). The construction of the sensitivity function has been performed starting from the reduced standard stars produced by ESOREX.

The reduced galaxy spectra can be seen in Fig. 1 (black lines). The three spectral windows of the X-Shooter arms (UVB, VIS, and NIR) are connected at ∼5600 and ∼10 200 Å (vertical dashed blue

lines) with the help of the available photometric data (see Section 5, green diamonds). Note that objects COSMOS-307881 and UDS 29410, due to their lower redshift, did not reveal any non-zero signal in the UVB region, which has not been included in the analysis. Nevertheless, for these two objects, we were able to measure UV indices such as Mg II at 2800 Å and Fe I(3000) as they fall in the VIS arm at these redshifts (see Table 3). In the NIR region, all the strong atmospheric absorptions have been masked by means of grey shading. Due to the low S/N of the data (typically lower than 10, cfr. Table 2), telluric absorptions cannot be properly removed, so we preferred to avoid any index measurement in the affected regions. For each galaxy, a representative model (Maraston & Strömbäck 2011, hereafter MS11) obtained from the analysis described in the following sections is shown (red line).

Note that in these figures and in the subsequent analysis, the observed spectra (black lines) have been binned to gain a higher S/N ratio, which after downgrading is about 4–7 per dispersion element (i.e. 1.8 Å in the UV and VIS arms and 2.0 Å in the NIR arm), depending on the spectral range. Indeed, the X-Shooter spectra, due to their high resolution, would be totally dominated by noise in case of such faint objects. The decrease in resolution allows us to sufficiently characterize the spectral features and make them suitable to be compared to models.

## 3 ANALYSIS

The wide spectral extension of the X-Shooter data allows the measurement of several spectral indices, which brings a wealth of information about a galaxy stellar content. Moreover, the high redshift of these galaxies allows us to access their rest-frame UV region.

Therefore, in this paper, we could explore for the first time the effect of simultaneously modelling the usual optical rest-frame region together with newly explored UV indices.

### 3.1 Measured indices

The measured index values are given in Table 3. Note that not all indices could be measured on each spectrum because the redshift
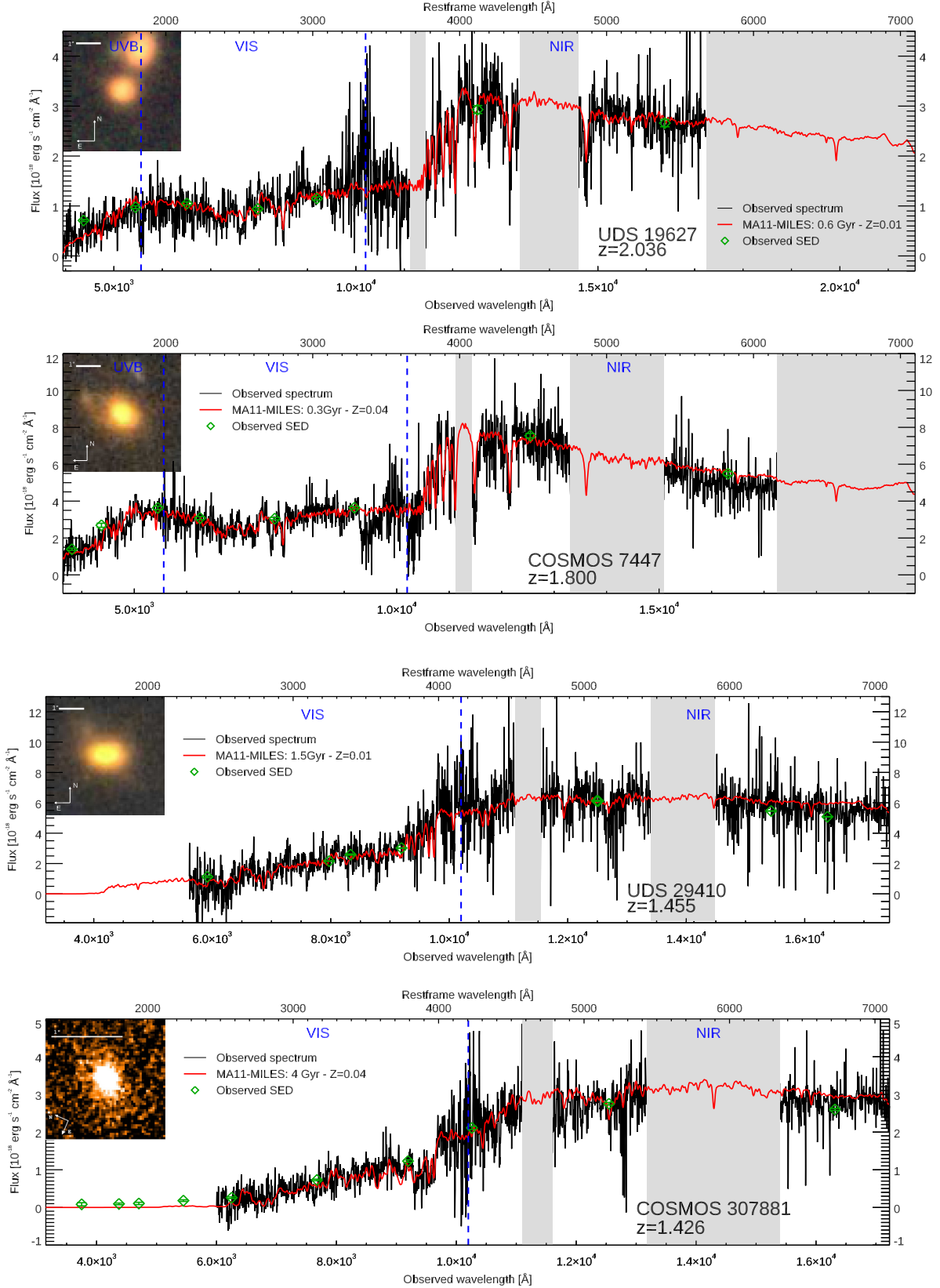
**Figure 1.** Observed spectrum of UDS-19627, COSMOS-7447, UDS-29410, and COSMOS-307881 ordered from the highest to lowest redshift, together with their respective *HST* images (van de Sande et al. 2013). The observed spectrum (black line) is compared with the available photometric data (green diamonds) and with a representative MS11 model (Maraston & Strömbäck 2011) (red lines). The vertical dashed blue lines indicate the connection between UVB–VIS and VIS–NIR arms at ∼5600 and ∼10 200 Å. In the NIR band, the strong atmospheric absorptions have been covered. The spectral resolution of the observed spectrum has been downgraded to match the MS11 one, i.e. FWHM = −2.55 Å rest frame.

**Table 3.** Spectral indices measured on the galaxy spectra and used in the analysis, ordered from the UV to the NIR. Blanks denote those indices that could not be measured due to poor spectral quality.

| Index | COSMOS-307881 | COSMOS-7447 | UDS-19627 | UDS-29410 |
|---|---|---|---|---|
| BL(1617) | – | – | $4.86 \pm 1.78$ | – |
| BL(1664) | – | $5.11 \pm 1.33$ | $4.11 \pm 1.88$ | – |
| BL(1719) | – | – | $-1.07 \pm 1.76$ | – |
| Fe II(2402) | – | $5.86 \pm 1.25$ | $4.51 \pm 2.13$ | – |
| BL(2538) | – | $4.35 \pm 1.30$ | $10.54 \pm 1.66$ | – |
| Fe II(2609) | – | $5.46 \pm 0.87$ | $6.92 \pm 1.26$ | – |
| Mg II | $14.00 \pm 2.79$ | $12.40 \pm 0.79$ | $13.02 \pm 1.28$ | $13.62 \pm 2.27$ |
| Mg i | $13.18 \pm 2.06$ | $2.50 \pm 0.82$ | $3.43 \pm 1.28$ | $10.41 \pm 1.83$ |
| Mg$_{wide}$ | $51.41 \pm 7.51$ | $19.63 \pm 14.52$ | $9.43 \pm 3.83$ | $8.79 \pm 6.66$ |
| Fe i(3000) | $9.60 \pm 3.72$ | – | $3.71 \pm 2.76$ | – |
| BL(3580) | $8.99 \pm 1.80$ | – | – | – |
| CN(3883) | $0.16 \pm 0.07$ | $0.07 \pm 0.03$ | – | $0.12 \pm 0.05$ |
| D4000 | $2.44 \pm 0.12$ | $1.450 \pm 0.06$ | $1.69 \pm 0.04$ | $1.75 \pm 0.04$ |
| CN(4170) | – | – | $-0.04 \pm 0.03$ | – |
| H$\delta_A$ | – | – | $4.93 \pm 1.26$ | – |
| H$\delta_F$ | – | $8.99 \pm 0.69$ | $4.87 \pm 0.87$ | – |
| H$\gamma_A$ | – | $10.68 \pm 0.86$ | $8.37 \pm 1.24$ | $6.30 \pm 1.43$ |
| H$\gamma_F$ | $-1.56 \pm 0.92$ | $7.91 \pm 0.54$ | $8.00 \pm 0.78$ | $5.22 \pm 0.94$ |
| G4300 | $6.52 \pm 1.12$ | – | $0.70 \pm 1.31$ | $3.44 \pm 1.38$ |
| Fe(4383) | $7.40 \pm 1.74$ | – | – | – |
| Ca(4455) | $1.06 \pm 0.83$ | – | – | – |
| Fe(4531) | $3.20 \pm 1.40$ | – | – | – |
| H$\beta$ | $2.52 \pm 0.93$ | – | – | $2.78 \pm 1.18$ |
| Fe5015 | $3.89 \pm 1.91$ | – | – | – |
| Mg$_b$ | $5.75 \pm 0.81$ | – | – | – |
| Fe(5270) | – | – | $1.61 \pm 0.76$ | – |

and the spectral quality (e.g. atmospheric absorption regions, telluric residuals, UVB–VIS–NIR arm connections) vary among the targets. This means that a specific analysis tailored to each galaxy needed to be performed, as will be discussed below. In order to understand the uncertainties in stellar population parameters derived with different sets of indices, we performed the same analysis on mock spectra with known population parameters and the same spectral quality as the data. These tests are described in Appendix A. We find that the use of different index sets does not affect the derived age and metallicity. A small improvement is noted when using a larger number of indices. We also show that in this young (<4 Gyr) age range, the addition of indices in the UV spectral range significantly helps the accuracy of the results.

Errors have been derived by means of a Monte Carlo approach. We added noise to the observed spectrum by perturbing the flux value at each pixel assuming a Gaussian error distribution. We performed 5000 Monte Carlo realizations. The flux error was derived from the noise spectrum that we extracted from the 2D spectrum at a location off target. Hence, the latter includes the sky residuals. We then measured the corresponding index values for each Monte Carlo realization and determined the statistical error from the width of the distribution of index measurements. Following our approach in Lonoce et al. (2015), we then divided this value by $\sqrt{2}$ since the observed spectrum already contains the intrinsic error. Systematic errors due to, for example, flux calibration are neglected since their level is well below the statistic uncertainties.

Within the optical rest-frame region, we could measure most of the well-known Lick/IDS indices (Worthey et al. 1994), following the band-pass definitions proposed by Trager et al. (2000a), together with the H$\delta$ and H$\gamma$ index definitions by Worthey & Ottaviani (1997). These indices, coupled with stellar population models sensitive to element abundance ratios (Thomas et al. 2011), allow the

derivation of $\alpha$-element enhancement (and other specific abundance ratios), which are key to derive star formation time-scales (Thomas et al. 2005).

In addition, we measured UV rest-frame spectral indices, which we could analyse using the models by Maraston et al. (2009), which have been tested on young star clusters in the Magellanic Clouds. The UV indices follow the definition by Fanelli et al. (1990) and Davidge & Clark (1994), as used in Maraston et al. (2009).

### 3.2 Stellar population models

For interpreting the observed Lick optical indices, we adopt the models by Thomas et al. (2011) (hereafter TMJ, for a Salpeter IMF), whose stellar index values are based on the MILES library (Sánchez-Blázquez et al. 2006) as from the index calibration by Johansson, Thomas & Maraston (2010). The underlying evolutionary population synthesis model is from Maraston (2005), which is consistently used also in the UV indices, the high-resolution model spectra, and the spectro-photometric fits (see below).

For the UV indices, we used the theoretical high-resolution models of Maraston et al. (2009), which is connected around 3700 Å with the models of Maraston & Strömbäck (2011, MS11[1]), in their version based on the MILES library, herein MS11-MILES UV extended (all for a Salpeter IMF). MS11 offer a suite of models with the same energetics (i.e. the same mass–luminosity relation on the main sequence and fuel consumption on the post-main sequence) and different stellar libraries. The reason for opting for the MILES version here is primarily to ensure consistency with the model Lick indices. Besides, the MS11-MILES allows the

---
[1] www.maraston.eu

widest metallicity range to be explored among the other available options.

We used the TMJ models for the Lick indices and the MS11 for the UV indices, homogenizing the model age grids as to cover from 0.1 to 12 Gyr at steps of 0.1 Gyr, and the metallicity grid to cover from $[Z/H] = -0.30$ to 0.30 at steps of 0.01. These ranges are those in common to both models so that no extrapolation is needed. The TMJ models provide index values at the MILES spectral resolution (i.e. 2.5 Å rest frame), while MS11 models provide the whole SED (we used the set at the MILES resolution here) on which any index can be measured. We measured the mid-UV indices (located below 4000 Å) from the MS11 SEDs for all available ages and metallicities and add this new mid-UV index set to the TMJ-based Lick indices at the correspondent age and metallicity. The finer grid described above was obtained in interpolation when necessary.

UV indices are indicators of the age and/or metallicity (see Maraston et al. 2009, for a description). The effect of element abundance ratios on these indices is not yet known. In this paper, we shall simulate the qualitative effect of an enhancement on Mg II(2800) and Mg I(2852) by applying the same differential index variation of the optical Mg$_b$(5175) as modelled in TMJ models for an $[\alpha/Fe] = 0.3$ (see Section 3.4 and Fig. 7).

In addition, we employ models including a UV upturn (by C. Maraston, based on the early modelling by Maraston & Thomas 2000) as used in Le Cras et al. (2016). The UV upturn is an enhanced flux in the ultraviolet observed in local massive galaxies and massive spiral bulges (see Maraston & Thomas 2000, and references therein). It is thought to be due to old, hot stellar components, which manage to expose high effective temperatures and become UV emitters. The astrophysical origin of such an evolution is still mysterious, as widely discussed by Greggio & Renzini (1990; see also Maraston & Thomas 2000), but the association to old (at least a few Gyr), metal-rich populations is an empirical fact. In order to simulate the variety of upturns observed in local galaxies and to allow for an exploration into the mysterious nature of the UV upturn, several models are calculated as a function of two parameters, namely the temperature (or temperature distribution) of the old UV components and the fuel consumption at those temperatures (as in Maraston & Thomas 2000). Table 1 in Le Cras et al. (2016) provides full details of the models. In Le Cras et al. (2016), the UV-upturn models were applied to a large sample of massive galaxies at $z \sim 0.7$–0.9 from SDSS-III, finding that a large fraction of them has spectra consistent with the presence of an upturn component. We also find as expected that the strength of such a component decreases with increasing redshift, following the rejuvenation of the stars. The $z \sim 1$ galaxies have ages and stellar masses (see Maraston et al. 2013 and Le Cras et al. 2016) that are similar to our lowest redshift galaxy, COSMOS-307881. Therefore, we shall probe whether the UV indices of this galaxy are consistent with the presence of an upturn.

### 3.3 Data-model comparison procedure

The analysis of spectral indices of high-$z$ ETGs must be carefully treated. Indeed, $z > 1.4$ ETGs contain rather young stellar populations (age $\sim$1–2 Gyr), and at these ages spectral indices change quickly for small changes of age and metallicity. This is not the case of local ETGs, which are old (age $>>5$ Gyr) and for which indices are stable in their dependence with stellar parameters (and also more degenerate, as well known).
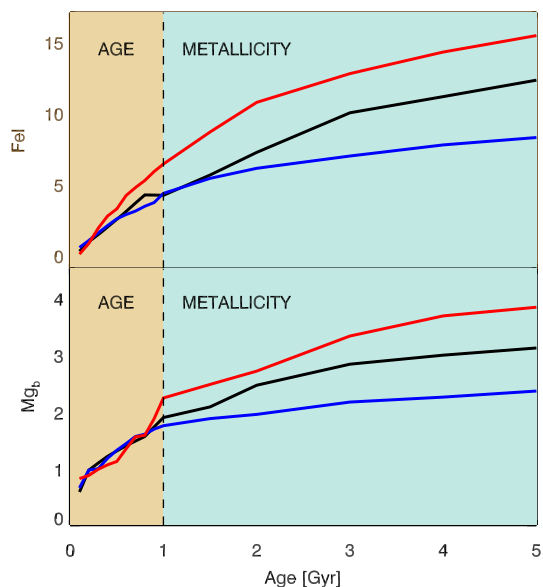


**Figure 2.** Examples of the different trends with age of two representative spectral indices, i.e. Fe i(3000) and Mg$_b$, for MS11 and TMJ models, respectively, for different stellar metallicities: subsolar (blue lines), solar (black lines), and supersolar (red lines). For ages <1 Gyr, both indices are solid *age* indicators, while for older ages they become better *metallicity* indicators.

Thus, we attempted a separation between more *age*-dependent and *metallicity*-dependent indices even if – it should be noted – it is not possible to perfectly disentangle the two parameters and the dominance of age and/or metallicity sensitivity depends on the explored age range. As an example, in Fig. 2, the trends of two indices, one UV index, Fe i(3000), and one Lick index, Mg$_b$(5175), are shown as a function of the age of the stellar population for three different stellar metallicity values: subsolar (blue lines), solar (black lines), and supersolar (red lines). We can see that for ages <1 Gyr both indices are solid *age* indicators showing a monotonic increase with age, with negligible metallicity effects, while for older ages the age dependence weakens (due to the milder evolution of the main sequence and red giant branch, e.g. Maraston 2005) and they become better *metallicity* indicators.

In addition (see Section 3), it has not been possible to measure all indices for all objects due to their different redshift and spectrum quality. This means that the sets of indices used in the analysis are different for each object.

Therefore, in order to avoid meaningless comparisons, the most efficient way to extract information from the many spectral indices was to perform a single-case analysis for each index and for each object. For each object, we classified each index as (mostly) *age* indicator or (mostly) *metallicity* indicator. Note that we have checked that if all indices were analysed simultaneously, the results would be less constrained (i.e. with larger uncertainties) since residuals of the age–metallicity degeneracy are left. A similar effect is also found if a separation between blue indices and Lick indices is adopted: the results point to the same parameter values but the degeneracy is more marked.

In Figs 3–6 for each galaxy the measured indices (black symbols with error bars) used in the final analysis are shown as a function of the most solid age-dependent broad index D4000, in comparison with the expectations of stellar population models (coloured lines
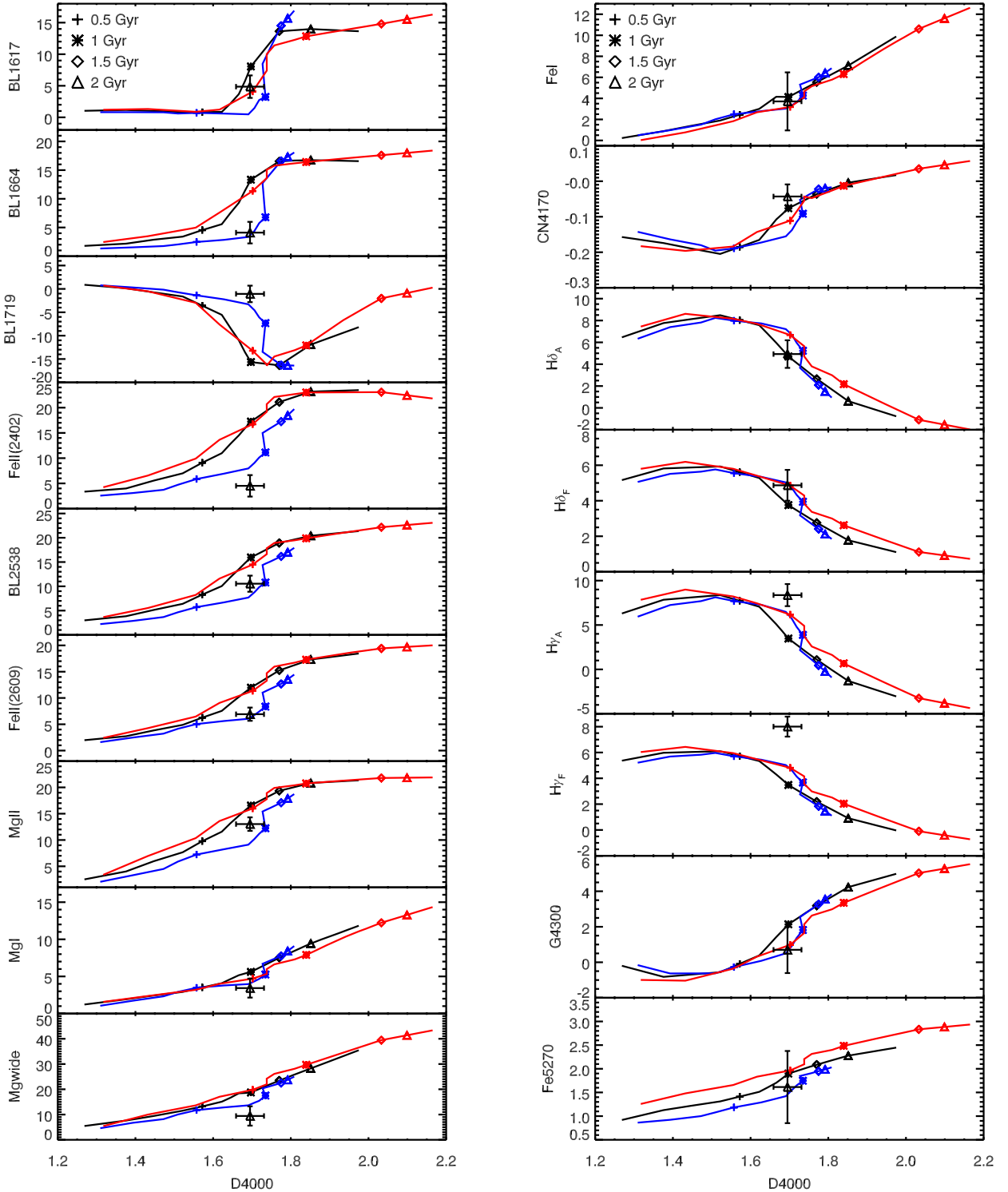
**Figure 3.** UDS-19627. Spectral indices as a function of the D4000 break, with measured data showed as black diamonds with error bars, are compared to stellar population models. The blue, black, and red lines refer to subsolar, solar, and supersolar metallicity, respectively. MS11 models are adopted for blue-UV indices and TMJ models for Lick indices. Ages run from 0.1 to the limit of the Universe age at this redshift; intermediate age values are highlighted with different symbols. Index values are corrected for the measured velocity dispersion (see Table 1).

for three different stellar metallicity values), MS11 models for blue-UV indices, and TMJ models for Lick indices.

For the analysis of each single object, we proceeded as follows. We first compared by means of a $\chi^2$ minimization the values of the set of *age*-dependent indices with the merged MS11–TMJ models

(described above) assuming ages from 0.1 Gyr to the limit of the age of the Universe determined by each galaxy's redshift, and metallicity from $[Z/H] = -0.30$ to 0.30. During these comparisons, index values have been corrected to remove the intrinsic broadening of the galaxy velocity dispersion, which affects absorption lines.
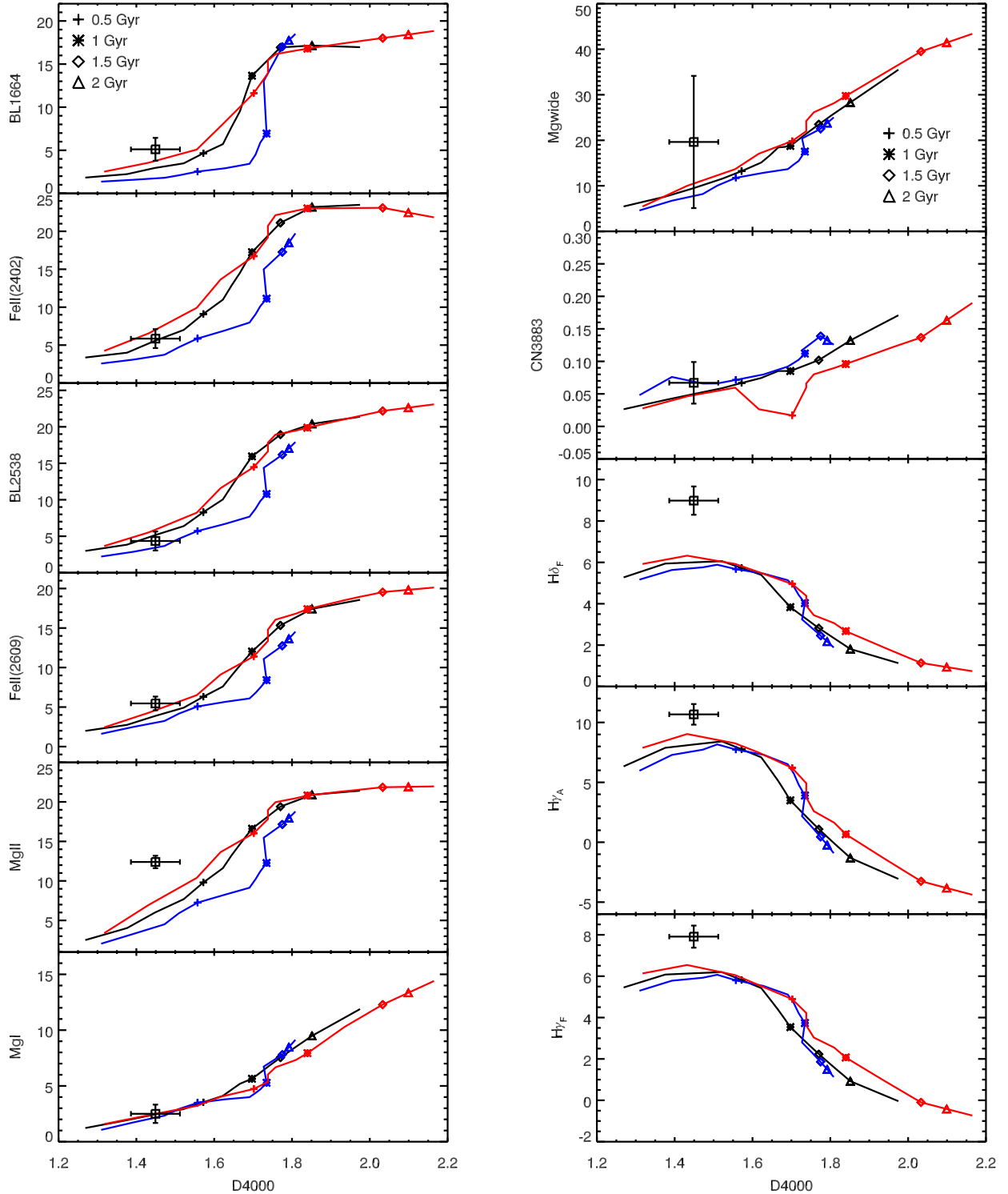
**Figure 4.** As in Fig. 3 for COSMOS-7447.

Index values were multiplied by correction factors, which were obtained by measuring indices on models broadened to the relevant velocity dispersions.

The best-fitting solution and the distribution of all fitting solutions with similar associated probabilities provided an estimate of the stellar population age with its error (Lonoce et al. 2015). The same procedure was repeated with the set of *metallicity*-dependent indices, but now including the constraint from the age analysis, i.e. ages are allowed to run only in the range indicated by the *age*-dependent indices, and the best-fitting metallicity value is obtained within this range. Results are summarized in Table 4. First of all, we notice that our spectral ages are in excellent agreement with the results obtained from the photometric fitting shown in Table 1, and discussed in Section 5.
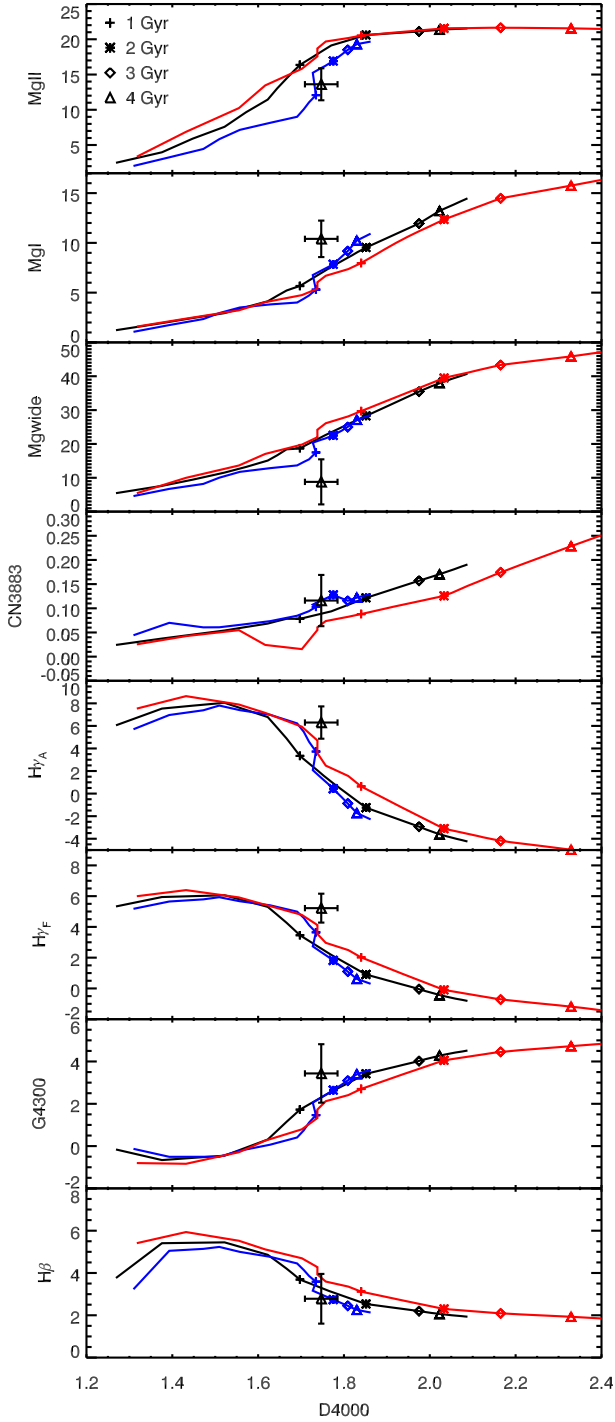
**Figure 5.** As in Fig. 3 for UDS-29410.

An estimate of $\alpha$-enhancement can be derived from suitable Lick indices using TMJ models, which are calculated for various values of this parameter. However, this measurement is challenging for distant galaxies due to the low S/N ratio of the spectra. In order to understand the feasibility of such a measurement given our data quality, we determine the stellar population parameters on mock spectra simulated to have the same S/N as the data, using the exact same set of indices as in the real data analysis (see Appendix A). We find that we are able to constrain the [$\alpha$/Fe] values for three out of four objects, albeit with rather large uncertainties. We estimated the $\alpha$-enhancement on our data by comparing the observed Lick indices with TMJ models again through a $\chi^2$ minimization process, with age running again from 0.1 Gyr to the limit of the age of the Universe at steps of 0.1 Gyr, covering a wider range of metallicities from [$Z/H$] = $-2.25$ to 0.67 at steps of 0.01, and with [$\alpha$/Fe] values in the range from $-0.30$ to $+0.50$ at steps of 0.01.

In Appendix B, we compare the best-fitting model indices (both from the combined MS11–TMJ and from the sole TMJ models) with the observed ones. We find that most of them agree well within $1\sigma$ and more generally they are consistent within $2\sigma$.

The resulting stellar population parameters are shown in Table 5. As expected, and also confirmed by the simulations described in Appendix A, it was not possible to constrain the stellar population parameters for object 7447 with only Lick indices as too few could be measured on the observed spectrum (see Table 3). From Table 5, it can be immediately seen that galaxy ages are well consistent between the two different analyses, which is an important result as galaxy ages are key to galaxy formation and evolution and also to use galaxies as cosmological probes (e.g. as cosmic chronometers, Moresco et al. 2016).

All results from Tables 4 and 5 will be discussed in more detail in Section 6.

A special case is that of COSMOS-307881 as already discussed in Lonoce et al. (2015). The previous paper by analysing only the Lick indices concluded for a very metal rich and $\alpha$-enhanced stellar population, as recalled in Table 5. The extended analysis presented here includes the information brought by bluer indices and it confirms the galaxy old age and high metallicity at the limits of the merged modelling (hereafter, for this galaxy, we will consider the metallicity value found from the Lick indices with TMJ models [$Z/H$] = $0.61^{+0.06}_{-0.05}$ as in Lonoce et al. 2015). At the same time, we noticed that some UV indices are not consistent with any of the adopted models (Fig. 6), showing systematically lower values that a metallicity cannot explain.

In order to find an explanation for these values, we further compare the UV indices with models including a UV upturn, in the next Section 3.4.

### 3.4 A possible UV upturn in COSMOS-307881

The emission in the UV region is dominated by the hotter component of a galaxy stellar population. Generally, the hottest component originates from the youngest stars (age <1 Gyr). However, also old stellar populations (age >1 Gyr) can become UV bright after a post-main-sequence phase of sufficient mass-loss (Greggio & Renzini 1990; Maraston & Thomas 2000). This phenomenon causes the so-called UV upturn (see Yi & Yoon 2004, for a review). The effect of the UV upturn on the spectrum shape is clearly visible in the far-UV (around 1000–2500 Å, see Burstein et al. 1988). Le Cras et al. (2016) show that spectral indices in the ~2500 Å region are also affected by this phenomenon [e.g. Mg ɪɪ(2800), Mg ɪ(2852), and Fe ɪ(3000)].

In a second step, we repeated the whole procedure excluding the contribution of Balmer-lines indices (e.g. H $\beta$, H $\gamma$, H $\delta$) in order to verify that possible residuals of star formation, which could affect these indices, or any younger minor stellar component would not alter the results. As can be seen in Table 4, the results obtained in the two cases, with and without the Balmer-lines indices, are completely consistent. This result may also be suggestive that Balmer lines are not crucial to constrain ages when all other spectral indices are available.
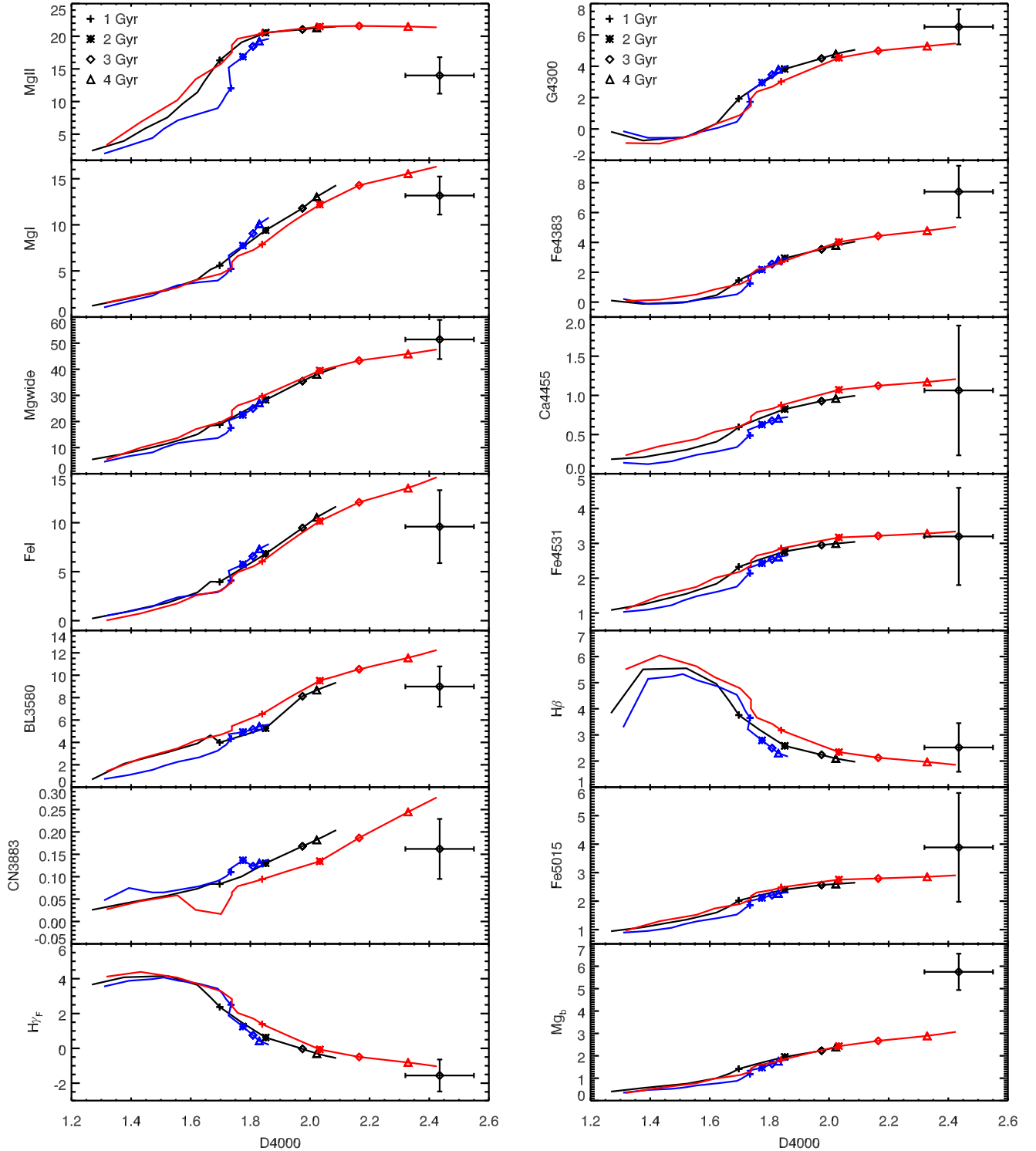
**Figure 6.** As in Fig. 3 for COSMOS-307881.

The origin of the UV upturn is still under debate. One of the most accredited possibilities, proposed by Greggio & Renzini (1990), is that post-main-sequence stars with an enough high-metallicity content do increase significantly the opacity in their stellar atmospheres, thus causing mass-loss during their horizontal branch phase. Consequently, the internal hot-

ter shells become exposed and are responsible for a UV emission.

COSMOS-307881 is the best candidate in our sample where to search for the presence of an UV upturn because it is the oldest galaxy and stellar populations need to age in order to possess low-mass stars that can become hot emitters. Moreover, this galaxy has

**Table 4.** Best-fitting values of age and metallicity with their reduced $\chi^2$ values obtained from the independent analysis of the set of *age*-dependent (first lines) and *metallicity*-dependent indices (second lines). The 'NO Balmer' columns refer to the analysis performed excluding the Balmer line indices (see the text).

| ID | Set of used indices | Age (Gyr) | (Z/H) | $\chi^2$ | Age (Gyr) NO Balmer | (Z/H) NO Balmer | $\chi^2$ |
|---|---|---|---|---|---|---|---|
| 19627 | [Mg i, Mg$_{wide}$, Fe i(3000), D4000, H$\delta_A$, H$\delta_F$, H$\gamma_A$, H$\gamma_F$, $G$ band] | $0.6 \pm 0.1$ | | 2.40 | $0.7 \pm 0.1$ | | 0.30 |
| | [BL(1617), BL(1664), BL(1719), Fe ii(2402), BL(2538), Fe ii(2609), Mg ii, CN(4170), Fe(5270)] | | $-0.30^{+0.1}_{-0.0}$ | 2.69 | | | |
| 7447 | [Mg i, CN(3883), D4000, H$\delta_F$, H$\gamma_A$, H$\gamma_F$] | $0.2^{+0.2}_{-0.05}$ | | 4.30 | $0.3 \pm 0.1$ | | 0.04 |
| | [BL(1664), Fe ii(2402), BL(2538), Fe ii(2609), Mg ii, Mg$_{wide}$] | | $0.26^{+0.04}_{-0.4}$ | 4.44 | | | |
| 29410 | [D4000, $G$ band, H$\beta$] | $1.8 \pm 0.3$ | | 0.21 | $1.8 \pm 0.4$ | | 0.30 |
| | [Mg ii, Mg i, Mg$_{wide}$, CN(3883), H$\gamma_A$, H$\gamma_F$] | | $-0.30^{+0.2}_{-0.0}$ | 2.94 | | $-0.30^{+0.1}_{-0.0}$ | 1.87 |
| 307881 | [CN(3883), D4000, H$\beta$] | $4.1 \pm 0.4$ | | 0.90 | $4.2 \pm 0.3$ | | 1.17 |
| | [Mg ii, Mg i, Mg$_{wide}$, Fe i(3000), BL(3580), H$\gamma_F$, $G$ band, Fe(4383), Ca(4455), Fe(4531), Fe(5015), Mg$_b$] | | $0.30^{+0.0}_{-0.14}$ | 2.40 | | $0.24 \pm 0.08$ | 2.56 |

**Table 5.** Results from the analysis of the sole Lick indices using TMJ models, which allow us to also determine the [α/Fe] parameter together with age and metallicity. For object 7447, it is not possible to retrieve the stellar parameters due to the too small number of available Lick indices (see also Appendix A).

| ID | Set of used indices | Age (Gyr) | [Z/H] | [α/Fe] |
|---|---|---|---|---|
| 19627 | [D4000, H$\delta_A$, H$\delta_F$, H$\gamma_A$, H$\gamma_F$, $G$ band, Fe(5270)] | $0.7^{+0.3}_{-0.2}$ | $-0.82^{+0.3}_{-0.6}$ | $-0.18^{+0.2}_{-0.12}$ |
| 7447 | [D4000, H$\delta_F$, H$\gamma_A$, H$\gamma_F$] | – | – | – |
| 29410 | [D4000, $G$ band, H$\beta$, H$\gamma_A$, H$\gamma_F$] | $1.2^{+0.6}_{-0.7}$ | $-0.70^{+0.2}_{-0.3}$ | $0.42^{+0.08}_{-0.1}$ |
| 307881 | [D4000, H$\gamma_F$, $G$ band, H$\beta$, Fe(4383), Ca(4455), Fe(4531), Fe(5015), Mg$_b$] | $4.1^{+0.5}_{-0.8}$ | $0.61^{+0.06}_{-0.05}$ | $0.45^{+0.05}_{-0.19}$ |

got the highest metallicity, which should also be a favouring factor for the onset of an upturn.

Most importantly, see Fig. 7, a discrepancy between the measured values of some UV indices [e.g. Mg ii(2800), Mg i(2852), and Fe i(3000)] and the models previsions that cannot be explained even assuming higher metallicity values has been found. In particular, Mg ii, Mg i, and Fe i values are lower than expected (black and red solid lines in Fig. 7), pointing towards younger ages that are not consistent with the indication of the D4000 and with the age resulted from the all-indices analysis.

Recently, Le Cras et al. (2016) have explored the occurrence of the UV upturn in a wide sample of massive, red and passive galaxies from $z\sim0.6$ up to $z\sim1$ from SDSS-III/BOSS (Dawson et al. 2013), finding that a significant fraction of the sample ($\sim$40 per cent) shows the signatures of this phenomenon. In order to reveal the UV upturn effect, the authors investigated UV spectral indices as well as full spectral fitting, using stellar population models calculated with different assumptions for the upturn component, as we recall in Section 3.2. The effect of the UV upturn starts at ages older

than 1 Gyr (see Le Cras et al. 2016, for further details). Here we compare these models with the Mg$_{wide}$, Mg ii(2800), Mg i(2852), and Fe i(3000), which Le Cras et al. (2016) find to be sensitive to the UV upturn effect and whose values for COSMOS-307881 cannot be reproduced by any standard model at whatever metallicity. The comparison is shown in Fig. 7.

It is clear that standard models (black and red lines) are not able to explain the measured values, independently of metallicity. For Mg ii(2800) and Mg i(2852), we also verified that an enhanced α/Fe ratio – as derived from the optical absorptions (Table 5) – does not help explaining the detected discrepancy. This is shown by models (dashed lines) in which we simulated the effect of [α/Fe]=0.3 on the UV indices by applying to these indices the differential index variation with [α/Fe] obtained from the TMJ models.

Only models including a UV upturn (green lines) are able to reach the observed values. With different tones of green, we display a range of calculations with ages >1 Gyr, a high 2Z$_\odot$ metallicity, and various assumptions for the temperature ($T_{\rm eff}$ = 25 000 and 35 000 K) and fuel consumption ($f$=6.5 × 10$^{-3}$, 6.5 × 10$^{-2}$/M$_\odot$) in
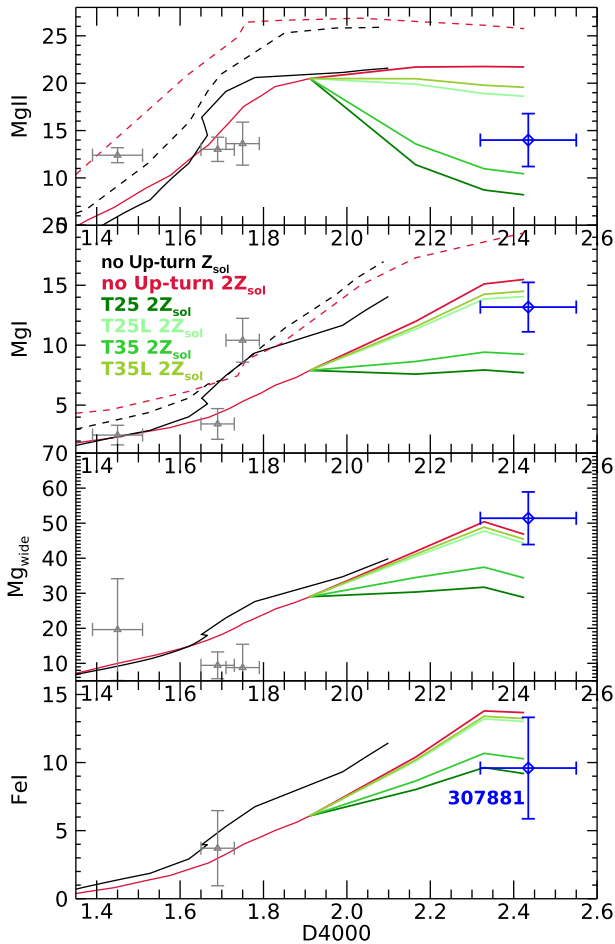
**Figure 7.** Mg II, Mg I, Mg$_{wide}$, and Fe I(3000) versus D4000 for COSMOS-307881 (blue symbols with error bars) compared to single-burst stellar population models with metallicities $Z_\odot$ (black) and $2Z_\odot$ (red). The solid and dashed lines refer to solar-scaled and supersolar values of [$\alpha$/Fe]. The green lines show models with UV upturns for various combinations of temperature ($T_{eff}$/K) and fuel ($f$/M$_\odot$). Details on upturn models can be found in Le Cras et al. (2016). The grey points show the index values for the other galaxies analysed in this work. No UV upturn is required to model the indices of these other galaxies.

the upturn. The best match would probably be achieved by a tuned mix of these two parameters.

The presence of a bright-UV old stellar population also helps explaining the detected [O II](3727 Å) weak emission, as already hinted in Lonoce et al. (2015). Indeed, by locating COSMOS-307881 on a BPT diagram involving [O II](3727 Å), [O III](5007 Å) (null flux), and H $\beta$ (in absorption) as shown in Thomas et al. (2013), we could classify this object as a LINER (low-ionization nuclear emission-line region) galaxy. From optical spectroscopic studies, it is known that a significant fraction of old elliptical galaxies belong to the LINERs population (Yan et al. 2006), although the ionization mechanism in LINERs is still under debate (Annibali et al. 2010; Belfiore et al. 2016). One of the most accredited scenarios is that photoionization by old post-asymptotic giant branch stars is responsible for the atomic excitations since their radiation is able to reproduce the observed emission-line ratios in LINERs (Trinchieri & di Serego Alighieri 1991). Our hypothesis is that the same old population that gives origin to the UV upturn also

contributes to the excitation of some residual gas in the interstellar medium of this ETG, thus causing the detected [O II] weak emission.

Fig. 7 also shows as grey points the index values for the other galaxies in our sample. It is clear that no UV upturn is required to model the indices of these other galaxies, which are all younger than COSMOS-307881. This result is then supportive of the idea that evolved, hot stellar components giving origin to the UV upturn pertain to old galaxies, where the typical evolutionary mass is small enough such that mass-loss can remove stellar envelope effectively and shift the effective temperature towards high values.

## 4 FULL-SPECTRUM FITTING

An additional analysis we performed was a full-spectrum fitting using the code FIREFLY (Wilkinson et al. 2017). Briefly, FIREFLY[2] (Fitting IteRativEly For Likelihood analYsis) is a full-spectrum fitting code based on $\chi^2$ minimization for comparing combinations of single-burst models (SSPs) to a given observed or mock spectrum (of a galaxy, a star cluster, etc.). FIREFLY iteratively fits these combinations, controlling them with a Bayesian information criterion until convergence in order to avoid overfitting. This code does not require any other prior than the assumed grid of population models. Dust attenuation is derived directly from the data before the fitting such that the continuum is corrected before the stellar population fitting is performed. This step not only helps fixing problems related to dust but also poor flux calibration of the data. The output of FIREFLY consists of age and metallicity (light- and mass-weighted), stellar masses and their partition into remnants, and $E(B - V)$ values, for the combined model fit as well as the individual SSP components. For a full description and details of the algorithm, and testing of the code performance on mocks of different S/N ratios, we refer the reader to Wilkinson et al. (2017), and for verification of its performance for a wide variety of galaxies and signal-to-noise ratios (down to S/N ∼5) to Comparat et al. (2017). We shall return on this when interpreting the results.

The models that FIREFLY used to perform the full-spectrum fitting for this work were the MS11-MILES UV-extended version of the MS11 models with a Salpeter IMF. Ages are constrained to be younger than the age of the Universe at each galaxy redshift, as we did in the spectral index and photometric analysis. Metallicity values run from [*Z/H*]=−0.3 to 0.3. With the data sample already at the same resolution as the models, the code (1) obtained the linear combination of the models that best fits the spectrum, (2) computed the contributions of the stellar populations, (3) converted the $\chi^2$ into probabilities, and (4) calculated the average properties and errors.

The mass- and light-weighted ages and metallicities obtained with FIREFLY for our ETG sample are given in Table 6, together with the reddening $E(B - V)$. The fits are shown in Fig. 8. The full spectral fitting describes the ETGs as young, except for COSMOS-307881, which results to be ∼4 Gyr old. Metallicities are slightly subsolar with the oldest galaxy having essentially a solar metallicity. There is little difference between light-weighted and mass-weighted quantities, which signifies that the duration of star formation is short and that galaxies are essentially passive or on the verge of becoming passive. The reddening is larger for the youngest objects and becomes small as the age increases, which is consistent with the absence of extended star formation. As we shall comment more extensively in the 'Discussion' section, these results are consistent with the output of the index analysis described in Section 3.

[2]www.icg.port.ac.uk/firefly

**Table 6.** `FIREFLY` full spectral fitting results: light- and mass-weighted age and metallicity and reddening $E(B-V)$. Note that for 19627 the lower bound of the error on the light-weighted metallicity is formally zero because the determination coincides with the bottom of the model grid.

| ID | Light-weighted age (Gyr) | Mass-weighted age (Gyr) | Light-weighted metallicity | Mass-weighted metallicity | $E(B-V)$ |
|---|---|---|---|---|---|
| 19627 | $0.19^{+0.12}_{-0.12}$ | $0.23^{+3.08}_{-0.04}$ | $-0.30^{+0.17}_{-0.00}$ | $-0.20^{+0.10}_{-0.10}$ | 0.29 |
| 7447 | $0.15^{+0.10}_{-0.03}$ | $0.21^{+0.98}_{-0.05}$ | $-0.12^{+0.12}_{-0.08}$ | $-0.18^{+0.18}_{-0.07}$ | 0.27 |
| 29410 | $1.10^{+0.93}_{-0.32}$ | $1.61^{+2.03}_{-0.55}$ | $-0.28^{+0.15}_{-0.02}$ | $-0.29^{+0.25}_{-0.01}$ | 0.08 |
| 307881 | $3.93^{+0.25}_{-0.43}$ | $4.89^{+0.11}_{-0.40}$ | $-0.05^{+0.04}_{-0.02}$ | $0.00^{+0.03}_{-0.02}$ | 0.14 |

We should stress that performing full spectral fitting of galaxy spectra with S/N < 10 is challenging. Wilkinson et al. (2017) show the results of extensive simulations on mock galaxy spectra with different S/N, star formation histories, reddening, etc. By glancing at their figs 8, 9, and 11, we learn that when fitting the spectra of galaxies with S/N = 5 and short star formation histories (single bursts and $\tau$-models with $\tau = 0.1$–1 Gyr) in the age regime relevant to our galaxies, metallicity can indeed be underestimated, while age is overestimated. Indeed, ages between a few hundreds of millions to a few billion years are most prone to the age/metallicity degeneracy. While we should not push these comparisons too quantitatively, the low S/N has an effect on the degradation of results from full spectral fitting. And yet, as we shall discuss in Section 6, the overall agreement between results from different techniques is encouraging.

## 5 PHOTOMETRIC FITTING

It is a general question whether broad-band photometry, which is what is usually available at high redshifts, is able to allow the determination of robust stellar ages of galaxies, and in general how ages determined via photometry or spectroscopy compare.

For this reason, we have performed spectrophotometry template fitting to the photometry of our four galaxies and determined their photometric ages, chemical composition, and stellar masses.

As in our previous works (Maraston et al. 2006, 2010), we use the `Hyperzspec` code (Bolzonella, Miralles & Pelló 2000) combined with ancillary scripts for the calculation of the stellar mass (Daddi et al. 2005; Maraston et al. 2006), and a selection of 32 sets of stellar population models based on the Maraston (2005) evolutionary population synthesis with a Salpeter IMF, spanning a variety of star formation histories including single-burst simple stellar populations, exponentially declining star formation histories ($\tau$-models), truncated star formation, and constant star formation. Each model star formation history spans a grid of 221 ages, and is available for four metallicities values between $\frac{1}{5}Z_\odot$ and $2Z_\odot$.

We performed the fitting for three options for the description of dust reddening, from no reddening to dust reddening following the Calzetti's law (Calzetti et al. 2000) or the so-called SMC law (Prevot et al. 1984) as available in `Hyperzspec`. The extinction parameter $A_V$ was allowed to vary between 0 and 3, in steps of 0.5. Furthermore, we used an age cut to retain only solutions older than 0.1 Gyr, which is commonly used in order to avoid age-dust degeneracy pushing the fits towards too low ages. It should be said that for these galaxies the setting or not of such a limit has no influence on the derived properties.

In performing the spectrophotometric fitting, we tried to use the same or similar bands for all the objects, depending on their availability. Simulations of photometric fitting varying the number

of filters and their wavelength extension (Pforr, Maraston & Tonini 2012; Capozzi et al. 2016) demonstrate that the fitting results depend on these parameters. We also excluded bands that at the putative redshift of the object would sample wavelengths longward the *K*-band rest frame (following Maraston et al. 2006). This is because standard population models such as M05 and BC03 do not model PAH or other effects longward *K*, hence the model fitting to those data is meaningless.

COSMOS 7447 (van de Sande et al. 2011) was fitted using bands *u* from CFHT/Megacam, *B*, *V*, *r*, *i*, and *z* from Subaru/Suprime-Cam, *J* and *K* from UKIDSS, and [3.6], [4.5], [5.8], and [8.0] μm from *Spitzer*/IRAC. For UDS 19627 (Toft et al. 2012), we used the same bands as COSMOS 7447, with the exclusion of channels [5.8] and [8.0]. On the other hand, compared to COSMOS 7447, UDS 29410 (Galametz et al. 2013) has band $R_c$ instead of *r* among the Subaru/Suprime-Cam bands, and also has *HST*ACS F606W and *HST*WFC3 F125W. Lastly, for COSMOS 307881, the same bands as for UDS 29410 were available with the exception of F606W and F125W.

Results are shown in Table 7, where we quote the best fit among all templates. From Fig. 9, we see that the photometric broad-band fitting releases galaxy ages that are in excellent agreement with what is obtained from the spectral analysis (compare also with Table 4). This is an important result considering that most future large galaxy surveys will essentially be based on photometry (e.g. *Euclid*). Also note that the photometric analysis suggests these galaxies to be passive, which is also consistent with what is derived from the spectra. Stellar masses, quoted for a Salpeter IMF, are in agreement with those determined by van de Sande et al. (2013) using Bruzual & Charlot (2003) models for a Chabrier IMF (we quote their masses augmented by 0.17, which is the conversion between Chabrier and Salpeter's IMFs; see Pforr et al. 2012). Fig. 10 shows the photometric fittings, the observed data being the red points with error bars. We note that the $\chi^2_r$ of COSMOS-307881 is rather high, probably due to the small errors of some of the photometric data. None the less, the other photometric points are still able to constrain the fits to the spectral age of ∼4 Gyr.

## 6 DISCUSSION

### 6.1 Comparison of results from fitting techniques

In spite of the low S/N of the spectra, we could perform several types of model fitting, finding interesting results for the stellar population content of these distant galaxies. The use of different techniques on the same objects also informs us on the most efficient approach and on the consistency of results, which will be useful in view of the advent of large telescopes and the JWST that will acquire a multitude of high-*z* galaxy spectra.
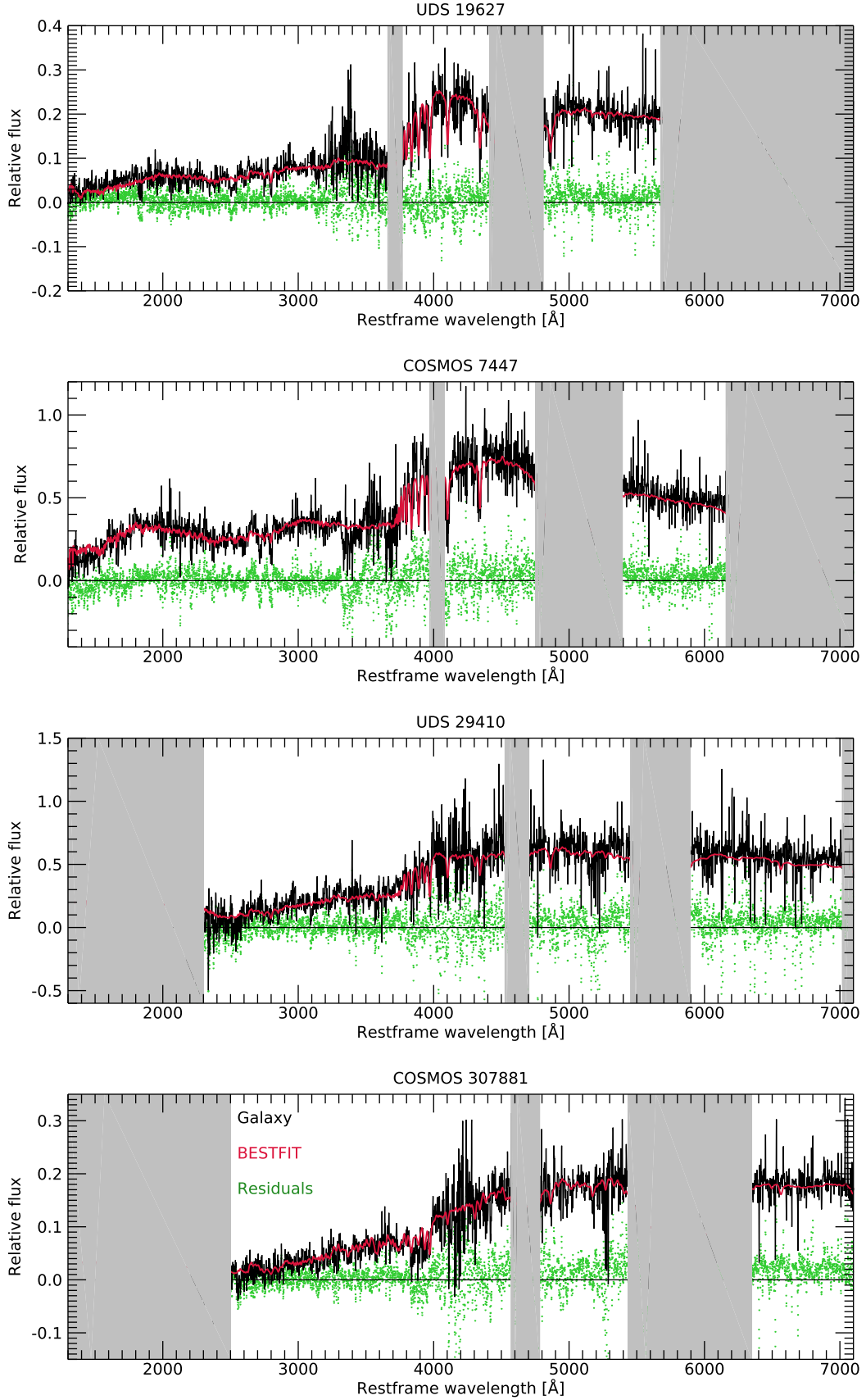
**Figure 8.** FIREFLY fits of the sample galaxies using UV-extended MS11-MILES models. The black spectrum represents the data, the red one is the best-fitting model, and green residuals. The grey areas are sections of the spectrum that were not considered in the fit.

**Table 7.** Results from photometric fitting (for a Salpeter IMF): stellar mass, age, metallicity, SFH, and reduced $\chi^2$. The values of stellar mass in brackets are from van de Sande et al. (2013) using Bruzual & Charlot (2003) models with a Chabrier IMF. The quoted constant ($+0.17$) is the conversion between Chabrier and Salpeter's IMFs from Pforr et al. 2012).

| ID | $\log \mathcal{M}_*$ ($M_\odot$) | Age$_{\text{phot}}$ (Gyr) | $Z_{\text{phot}}$ | SFH$_{\text{phot}}$ | $\chi^2_r$ |
|---|---|---|---|---|---|
| 19627 | 11.34 (11.24 + 0.17) | 0.7 | 0.004 | SSP | 7.971 |
| 7447 | 11.36 (11.27 + 0.17) | 0.2 | 0.04 | SSP | 2.649 |
| 29410 | 11.69 (11.29 + 0.17) | 2.4 | 0.004 | SSP | 13.418 |
| 307881 | 11.65 (11.50 + 0.17) | 4.5 | 0.02 | $\tau = 0.3$ | 24.990 |

Let us first compare the results obtained with different techniques and assess their consistency.

Table 8 provides a summary of the final derived stellar population parameters according to the different techniques, from spectral indices through full spectral fitting to photometric fitting. It should be noticed that the parameters from the indices given in Table 8 are drawn from both Tables 4 and 5: ages are better constrained using all indices (UV + Lick), whereas metallicities are better derived from only Lick indices and the TMJ models. The $\alpha$-enhancement is derived from the Lick indices plus the TMJ models only. The comparison between the same parameters as derived with the three methods is visualized in Fig. 9.

The parameter that we could determine most robustly turned out to be the galaxy age, which appears to be very stable independently of the fitting technique. Ages from spectral indices, full spectral fitting, and broad-band photometry fitting are all very similar. This is an important result for performing galaxy evolution with large photometric surveys.

The metallicities [$Z/H$] derived from indices show quite a scatter from very subsolar ([$Z/H$]=−0.82) to the very high value of COSMOS-307881 ([$Z/H$]=0.61). Two galaxies have subsolar metallicities, and two galaxies have supersolar metallicity. Interestingly, the metallicities derived with the other two methods, although being different in absolute values (but consider the errors), do display the same trend, namely the same galaxy is found to be solar(subsolar) independently of the technique. An exception is COSMOS-7447 for which the result from the full spectral fitting value is in disagreement with those from the other two methods. COSMOS-307881 is found to be very metal rich according to spectral indices, while the other techniques agree towards solar metallicity.

Regarding the $\alpha$-enhancement, the two oldest galaxies have an [$\alpha$/Fe] $\sim +0.4$, consistent with massive ellipticals in the local Universe (e.g. Thomas et al. 2010) and at high redshifts (Onodera et al. 2012; Kriek et al. 2016), one galaxy is solar scaled, and for object 7447 this parameter could not be determined as we only had Balmer line measurements for it.

In summary, ages are robust and consistent, and metallicities show a similar trend. If we consider the cosmic distance and the low S/N of our data, the general agreement between results from various methods is encouraging.

## 6.2 Formation epochs and evolution to $z \sim 0$

As noted before, the parameter we could determine most robustly turned out to be the galaxy age, which resulted to be very stable independently of the adopted fitting.

Galaxy ages show an approximately monotonic behaviour with redshift, with the oldest galaxy being found at the lowest redshift (Fig. 11).

From the age estimates, we can derive the epochs of stellar formation. With the exception of the object COSMOS-307881 that has a redshift of formation $z_{\text{form}} \sim 5$, the other three galaxies have formed the bulk of their stars around $z_{\text{form}} \sim 2$–2.5, i.e. around the peak of the cosmic star formation (Madau & Dickinson 2014, and references therein). The high formation redshift for COSMOS-307881 suggests that this galaxy is a descendant of massive, $z \sim 3$–5 objects recently found by various authors (e.g. Glazebrook et al. 2017; Guarnieri et al. 2019; Santini et al. 2019).

The expected evolution of these galaxies from the epochs of observation to $z \sim 0$ can be explored by comparing the stellar population properties derived from this analysis with the results from the local Universe, i.e. by using local scaling relations between stellar parameters and the velocity dispersion. As comparison sets, we adopt the results by Thomas et al. (2010) based on the Sloan Digital Sky Survey data and those for the sample of $\sim$50 local ETGs by Spolaor et al. (2010). In both cases, the data were analysed using spectral indices and $\alpha$-sensitive models as we do here (see Fig. 12). In particular, in Thomas et al. one set of parameters is given, which corresponds to an intermediate value between the centre and one effective radius, while in Spolaor et al. the stellar parameters are measured both in the inner core (within a radius of $r_e/8$) and at the effective radius ($r_e$, considered as the mean values of the global stellar population; see Spolaor et al. 2010). This double information is precious because it not only provides an indication of the parameters gradients within the galaxies, but also gives us a tool to understand if the compact galaxies of our sample will resemble the centres of local elliptical (Naab, Johansson & Ostriker 2009; Huang et al. 2013) or will they manage to enlarge their radius without changes in their stellar content.

In Fig. 12, the stellar properties age (top panels), metallicity (middle panels), and $\alpha$-enhancement (bottom panels) are plotted as a function of the velocity dispersion at $1r_e$ (left-hand panels) and at $r_e/8$ (right-hand panels). Our objects are labelled with green symbols. The central ($r_e/8$) values of $\sigma$ for the galaxies of our sample have been derived from the global ones assuming the formula by Cappellari et al. (2006). The black crosses in the right-hand panels refer to the central values ($r_e/8$) of the local sample of Spolaor et al. (2010), and the solid black lines show the scaling relations. The blue crosses and lines in the left-hand panels analogously refer to the mean values. Typical error bars are shown in the upper left corner of each panel.

The values for the high-$z$ galaxies (green diamonds in Fig. 12) lie into the right region of all plots, which corresponds to the largest velocity dispersions. This is not surprising because our sample is
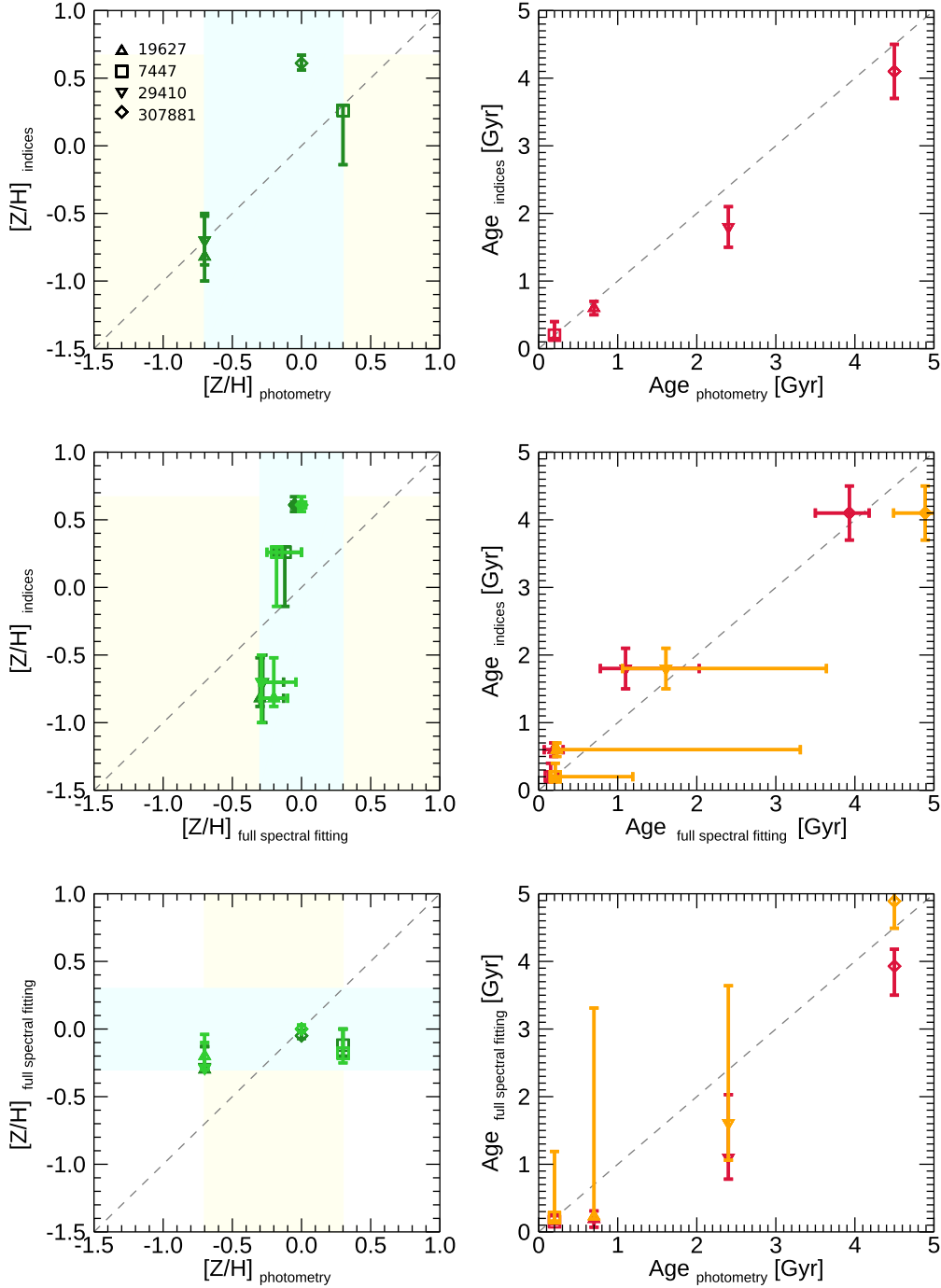
**Figure 9.** Age and metallicity values derived from index analysis (Table 8), full spectral fitting analysis (Table 6), and photometric analysis (Table 7). Upper panels: index analysis versus photometry; middle panels: index analysis versus full spectral fitting; lower panels: full spectral fitting analysis versus photometry. For full spectral fitting analysis, we report both light-weighted quantities (age red and metallicity dark green) and mass-weighted quantities (age orange and metallicity light green). The shaded areas show the metallicity ranges of the models used in each method.

composed by compact ETGs that are typically found to be denser than local objects (Trujillo et al. 2009). Indeed, as shown in Table 1, the dynamical masses of our objects are consistent with those of local ellipticals.

In order to compare the ages obtained at $z > 1.4$ with those in the local Universe, we have aged the stellar populations of our objects assuming passive evolution (Fig. 12, top panel). Ageing is indicated by vertical grey arrows pointing towards $z \sim 0$ (orange

symbols). It can be seen that our high-$z$ objects will evolve on to the local scaling relation. We can then conclude that the star formation histories of the galaxies of the distant sample are consistent with a star formation that started at $z \sim 2$ ($\sim 5$ for COSMOS-307881) followed by passive evolution. We can also conclude that the four distant objects are likely precursors of local ETGs.

In the middle panel of Fig. 12, we compare our derived metallicities with the local ones. A larger scatter with respect to the
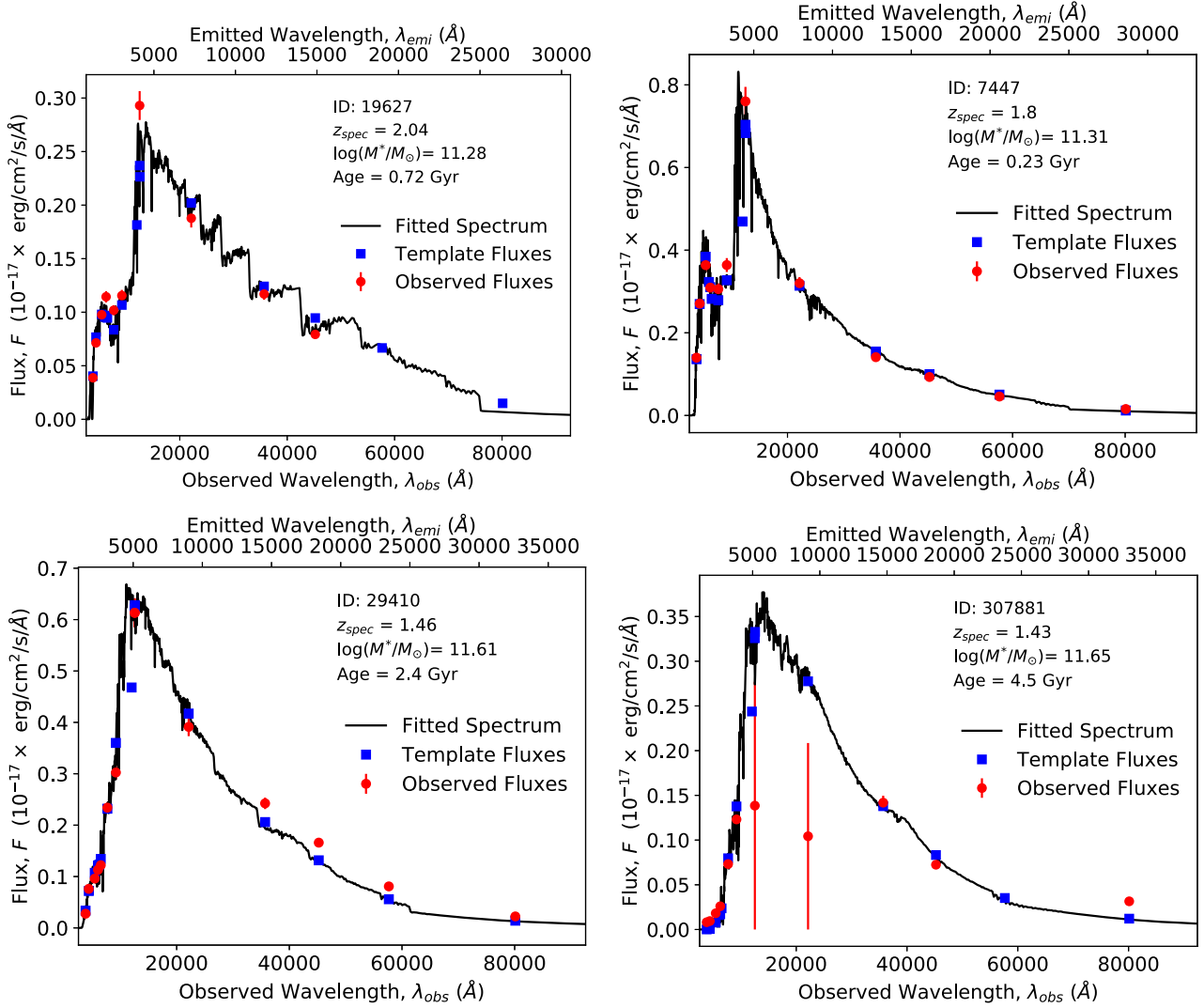
**Figure 10.** Results of photometric model fitting. Galaxies are ordered as decreasing spectroscopic redshift from top left to bottom right. In each panel, the observed data (red circles with error bars) are shown together with the template fluxes (blue squares) to which the data have been fitted to (in the same filters) and also the best-fitting model spectrum (solid black line). The derived properties age (Gyr) and stellar mass (in log and solar units) are labelled, along with the galaxy ID and the spectroscopic redshift.

**Table 8.** Summary of fitting results for all adopted techniques. From left to right, age (Gyr), [Z/H], and [α/Fe] from spectral indices, full spectral fitting (using light-weighted quantities), and photometry fitting. The [α/Fe] for COSMOS-7447 is not constrained since only Balmer lines are usable for this galaxy.

| ID | $Age_{IND}$ (Gyr) | $[Z/H]_{IND}$ | $[\alpha/Fe]_{IND}$ | $Age_{FSF}$ (Gyr) | $[Z/H]_{FSF}$ | $Age_{PHOT}$ (Gyr) | $[Z/H]_{PHOT}$ |
|---|---|---|---|---|---|---|---|
| 19627 | $0.6 \pm 0.1$ | $-0.82^{+0.3}_{-0.06}$ | $-0.18^{+0.20}_{-0.12}$ | $0.19^{+0.12}_{-0.12}$ | $-0.30^{+0.17}_{-0.00}$ | 0.7 | $-0.7$ |
| 7447 | $0.2^{+0.2}_{-0.05}$ | $+0.26^{+0.04}_{-0.40}$ | $-$ | $0.15^{+0.10}_{-0.03}$ | $-0.12^{+0.12}_{-0.08}$ | 0.2 | $+0.30$ |
| 29410 | $1.8 \pm 0.3$ | $-0.70^{+0.2}_{-0.3}$ | $+0.42^{+0.08}_{-0.10}$ | $1.10^{+0.93}_{-0.32}$ | $-0.28^{+0.15}_{-0.02}$ | 2.4 | $-0.7$ |
| 307881 | $4.1 \pm 0.4$ | $+0.61^{+0.06}_{-0.05}$ | $+0.45^{+0.05}_{-0.19}$ | $3.93^{+0.25}_{-0.43}$ | $-0.05^{+0.04}_{-0.02}$ | 4.5 | $+0.0$ |

age diagram is seen in the [Z/H] versus σ plane, even if it is of the order of the local sample one. The four galaxies point to two distinct behaviours: COSMOS-307881 and COSMOS-7447 seem to lie on the local scaling relation related to the central values, while UDS-19627 and UDS-29410 on the one built with the local mean values.

Different scenarios may be envisaged for the formation and evolution of these galaxies. As far as COSMOS-307881 is concerned,

its high metallicity value is expected from the local scaling relation at high velocity dispersion. A possible explanation proposed by the model of Pipino & Matteucci (2004) is that high-mass objects formed in a rapid star formation burst with the consequent increasing of the star formation efficiency and thus of the metal production. This scenario is also supported by the high value of the α/Fe ratio of this object (as shown in Fig. 12, bottom panel), which is tightly connected with the star formation time-scale as modelled
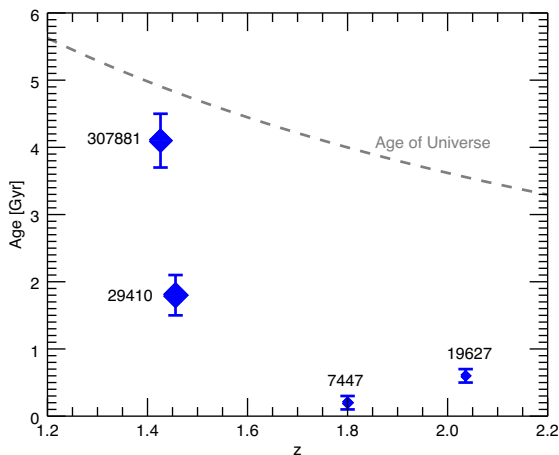
**Figure 11.** Galaxy ages (in Gyr) versus spectroscopic redshift, with the age of the Universe for a Planck (2013) cosmology indicated as a dashed line. The age of the oldest galaxy lies close to the age of the Universe at the given redshift. Younger galaxies lie at progressively higher redshift.

by Thomas et al. (2005), which in this case results to be short ($\Delta t \sim 0.1$ Gyr). Comparable supersolar gaseous metallicities are, for example, observed in quasars at $z > 4$ (Juarez et al. 2009). Such metallicity values in the local Universe are not found in the global values of local ellipticals, but only in their centres as observed in many works focused on metallicity gradients of local ETGs (Trager et al. 2000a; Spolaor et al. 2008; Martín-Navarro et al. 2015). This means that probably COSMOS-307881 will experience minor merging events with lower metallicity systems during its evolution towards $z = 0$, which are able to dilute both the velocity dispersion and the chemical content (Naab et al. 2009). Indeed, low-mass systems (as dwarf galaxies) are expected to contain low-metallicity stars as it is observed in the local mass–metallicity relation (Thomas et al. 2005). This interpretation is shown in Fig. 13 upper panel: COSMOS-307881 probably comes from an even more metal rich position (orange arrow) and will probably evolve in the direction (cyan arrow) of the cores local scaling relation (black line), decreasing both its metal content and its velocity dispersion by means of mass accretion.

Different scenarios must be invoked for the other three objects, which, although as massive and dense as COSMOS-307881, seem to be featured by a lower metallicity. COSMOS-7447 shows a supersolar metallicity, but its large error bar makes it consistent also with subsolar values. A possibility similar to the previous one is that, given their high mass and the arguments previously exposed, also these galaxies have formed in a short burst at $z \sim$ 2–2.5 from high-metallicity gas, but their metal content has been already diluted by merging events that happened soon after the formation and that involved the whole galaxy, not only its external regions. This scenario is outlined in Fig. 13 upper panel: The orange arrows show the direction from which the sample galaxies (green diamonds) are formed in the [*Z/H*] versus $\sigma$ plane, and the cyan arrows show their possible future evolution.

Still adopting the merging scenario, we can also suppose that these three ETGs have formed from a metal-poor nebular gas as that of Lyman-break galaxies (LBGs), observed at $z \sim 3$ as less metal enriched than local star-forming galaxies (Mannucci et al. 2009). Indeed, LBGs could be the progenitors of $z \sim 1$ compact ETGs (Williams et al. 2014). In this case, the sample ETGs are formed in the position where they are observed in the [*Z/H*] versus

$\sigma$ plane (Fig. 13, upper panel, not considering the orange arrows), and their evolution will push them towards the region occupied by lower density systems, thanks to minor merging events with subsolar to solar metallicity systems (cyan arrows).

Another scenario is that of gas fuelling (Fig. 13, bottom panel): Supposing again that these galaxies started their evolution from a metal-poor stellar composition (and, e.g. being the descendant of LBGs), residual cold gas streams reaching the inner part of ETGs would activate new star formation events prolonged in time, thus increasing the metal content in the galaxy centres. Indeed, it seems that field ETGs are able to retain gas coming from evolving stars, which is able to form new generation of metal-rich stars (Peebles 2002). This is consistent with the results obtained in Lonoce et al. (2014), where the constant presence of small amounts of young stars in $z \sim 1$ ETGs is observed. This process, as shown in Fig. 13 (bottom panel) with the same notation as before, would leave the galaxies with metallicity (and age) gradients, as it is observed in the local Universe (Spolaor et al. 2010; La Barbera et al. 2012; Goddard et al. 2017). Cold gas streams with prolonged star formation would lower the [$\alpha$/Fe] value, as we observe in UDS-19627, but not in COSMOS-307881 and UDS-29410 (see Fig. 12 lower panels). Moreover, this scenario cannot explain the evolution of COSMOS-307881, as it is unlikely that its metallicity will further increase.

The minor-merging scenario is expected to trigger central star formation by funnelling cold gas towards galaxy centres. The gas is consumed just after falling in the potential well of the galaxy, and the star formation triggered by this kind of event is expected to be bursty. In case of dry mergers, no star formation is expected. On the other hand, the gas-funnelling scenario foresees the presence of neutral cold gas filaments between galaxies, feeding a low but continuous star formation activity. Discriminating between the two scenarios would be possible by means of observations searching for molecular gas around high-redshift ETGs with ALMA. Deep searchings for molecular gas in high-redshift galaxies have been recently carried out (Decarli et al. 2016), but present surveys usually aim at studying star-forming galaxies for which the amount of molecular gas is much higher than the one expected around quiescent galaxies. Indeed, the deepest ALMA observation able to quantify the molecular gas content of a non-star-forming galaxy at $z > 1$ (Bezanson et al. 2019) did not reach a reliable detection, providing an upper limit to the molecular H2 gas mass of $1.1 \cdot 10^{10}$ M$_\odot$ in a post-starburst galaxy at $z = 1.5$. The more promising way to distinguish between the two scenarios seems to be spatially resolved studies of the stellar content within quiescent high-redshift galaxies, which could be obtained by the next generation of large telescopes (e.g. JWST, E-ELT, and GMT).

Finally, from the bottom panels of Fig. 12, we obtain indications on the star formation time-scales of those galaxies for which the $\alpha$/Fe ratio could be derived, i.e. COSMOS-307881, UDS-19627, and UDS-29410. As already mentioned, high values of [$\alpha$/Fe] imply short star formation time-scales since the lack of Fe-peak elements is a sign that supernovae type Ia did not had enough time to explode before the star formation quenching. Massive systems are expected to show high values of $\alpha$/Fe (i.e. short star formation time-scale), as indicated by the local mass–[$\alpha$/Fe] scaling relation. This is the case for COSMOS-307881 and UDS-29410, which are consistent with the local scaling relation (see Fig. 12, bottom panel), confirming the expectations of Thomas et al. (2005) and Pipino & Matteucci (2004). UDS-19627 instead shows a subsolar value of [$\alpha$/Fe] in contrast with the expectations. However, its value is consistent within the observed scatter of the local scaling relation, i.e. similar massive local ETGs with low [$\alpha$/Fe] do exist.
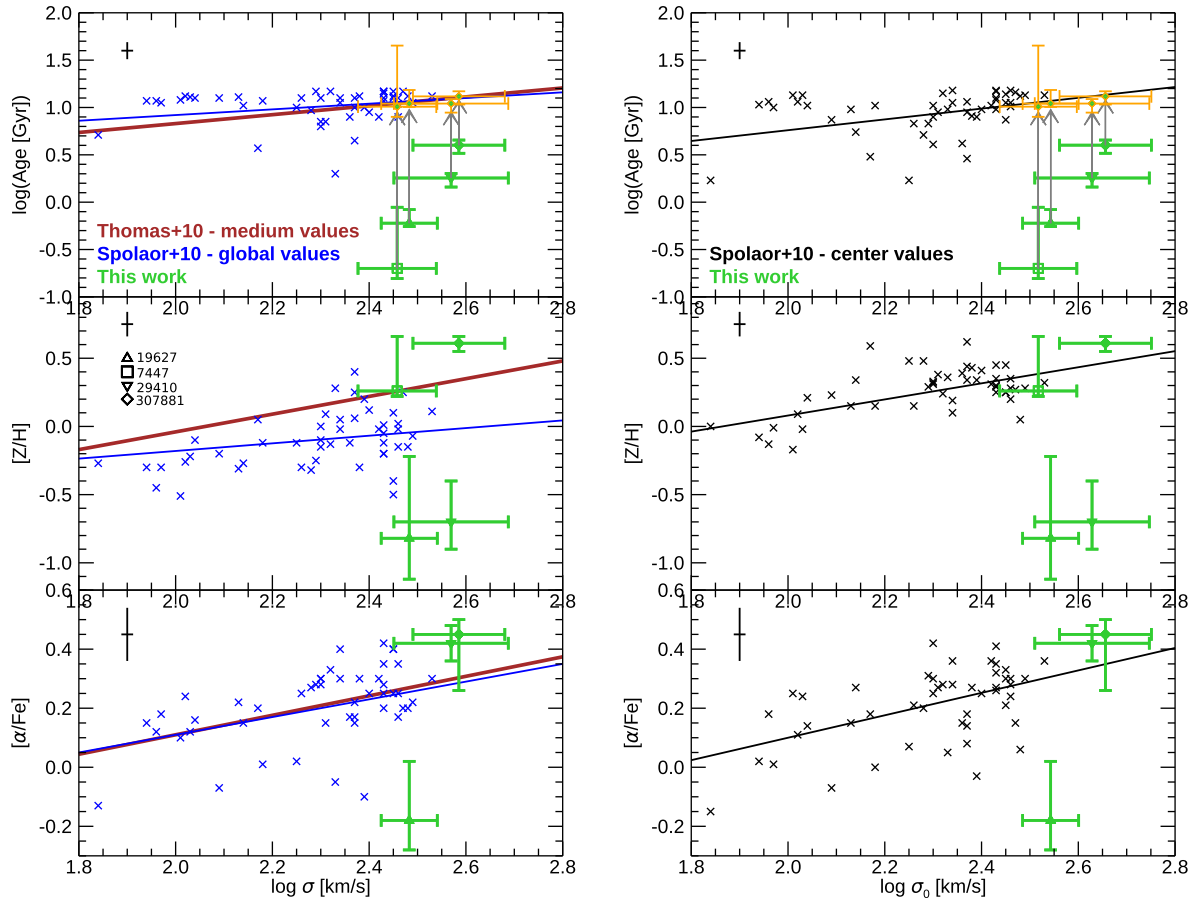
**Figure 12.** Comparison with local scaling relations of age (top panels), metallicity (middle panels), and $\alpha$-enhancement (bottom panels) as a function of the velocity dispersion at $1r_e$ (left-hand panels) and at $r_e/8$ (right-hand panels). The brown lines refer to the local scaling relations from Thomas et al. (2010). The black and blue crosses are the central ($r_e/8$) and mean values for the local sample of ETGs by Spolaor et al. (2010) with the correspondent scaling relation shown as black and blue lines, respectively. Typical error bars are shown in the upper left corner of each panel. Our galaxies are shown as green symbols. Ages after assuming passive evolution are shown in orange, and the symbols are connected with grey arrows.

## 7 SUMMARY AND CONCLUSIONS

In this paper, we present new age, metallicity, and [$\alpha$/Fe] estimates for four individual ETGs at $z > 1.4$ in the COSMOS and UDS fields. These measures have been performed thanks to the unique possibility of analysing many spectral indices from the UV to the near-IR given by the X-Shooter spectra, which cover a wide spectral range with high spectral resolution. In particular, besides the optical Lick indices, we have exploited UV spectral indices (down to $\sim$1500 Å rest frame). The large number of indices we could measure significantly helped in disentangling the residual age–metallicity degeneracy in the comparison with stellar population models. The addition of the UV indices helps with age determinations.

For obtaining the galaxy stellar population parameters, we have employed three popular techniques, namely fitting of individual absorptions, full spectral fitting, and photometric fitting, and we have compared the results.

In case of spectral indices, galaxy-tailored analyses have been performed. Galaxy ages have been constrained with a mean error of $\sigma_{\rm Age} \sim 0.3$ Gyr, stellar metallicities with a mean $\sigma_{[Z/H]} \sim 0.24$, and we obtained the $\alpha$/Fe abundance ratio for three out of four objects.

By using population models including UV-bright, evolved stellar components (Le Cras et al. 2016), we infer the presence of a UV

upturn in the oldest, most massive and most metal-rich galaxy of the sample, COSMOS-307881. Only UV-upturn models were able to explain the strong UV indices of this galaxy. This is the highest redshift detection of the UV upturn with spectroscopic measurements.

With the same spectroscopic data and public broad-band photometry, we have derived ages and metallicities from full spectral fitting using the FIREFLY code and from broad-band SED fitting using the HyperZ code. Noticeably, we found an excellent agreement between galaxy ages determined via indices, full spectral fitting or broad-band colours. Even if for just a few objects, this is an important result that will be useful to exploit data from future large photometric surveys, as *Euclid* or LSST, for the vast majority of which spectra will not be available.

We compared the stellar population properties of the high-$z$ galaxies with those measured in the local Universe. We find that our galaxies will evolve on the local scaling relations following pure passive evolution.

Additionally, we speculate on possible formation and evolution scenarios for our objects, being aware that higher S/N spectra will be needed to confirm metallicity and element ratios.

In the future, it will be very interesting to repeat our analysis on a larger sample of high-redshift ETGs.
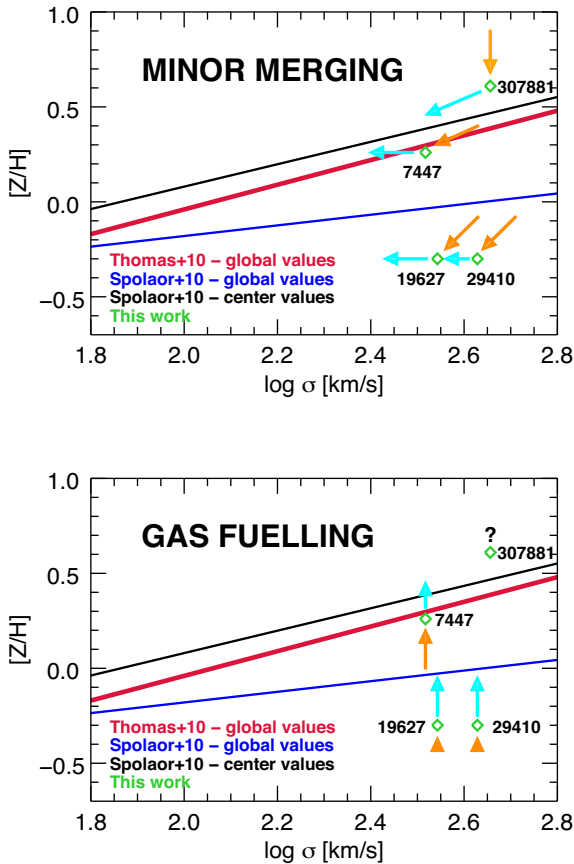
**Figure 13.** Mass–metallicity relation: two possible scenarios for the evolution of the sample galaxies (green diamonds) in comparison with the local relation of Spolaor et al. (2010) (see Fig. 12). Upper panel: minor merging scenario. Bottom panel: gas fuelling scenario. The orange arrows refer to the formation and the cyan arrows to the evolution of these galaxies.

## REFERENCES

Allanson S. P., Hudson M. J., Smith R. J., Lucey J. R., 2009, ApJ, 702, 1275
Annibali F., Bressan A., Rampazzo R., Zeilinger W. W., Vega O., Panuzzo P., 2010, A&A, 519, A40
Belfiore F. et al., 2016, MNRAS, 461, 3111
Bernardi M., Sheth R. K., Nichol R. C., Schneider D. P., Brinkmann J., 2005, AJ, 129, 61
Bezanson R., Spilker J., Williams C. C., Whitaker K. E., Narayanan D., Weiner B., Franx M., 2019, ApJ, 873, L19
Bolzonella M., Miralles J.-M., Pelló R., 2000, A&A, 363, 476
Bruzual G., Charlot S., 2003, MNRAS, 344, 1000
Burstein D., Bertola F., Buson L. M., Faber S. M., Lauer T. R., 1988, ApJ, 328, 440
Calzetti D., Armus L., Bohlin R. C., Kinney A. L., Koornneef J., Storchi-Bergmann T., 2000, ApJ, 533, 682
Capozzi D., Maraston C., Daddi E., Renzini A., Strazzullo V., Gobat R., 2016, MNRAS, 456, 790
Cappellari M. et al., 2006, MNRAS, 366, 1126

Chabrier G., 2003, PASP, 115, 763
Clemens M. S., Bressan A., Nikolic B., Alexander P., Annibali F., Rampazzo R., 2006, MNRAS, 370, 702
Comparat J. et al., 2017, preprint (arXiv:1711.06575)
Cresci G., Mannucci F., Curti M., 2019, A&A, 627, A42
Daddi E. et al., 2005, ApJ, 626, 680
Davidge T. J., Clark C. C., 1994, AJ, 107, 946
Dawson K. S. et al., 2013, AJ, 145, 10
Decarli R. et al., 2016, ApJ, 833, 70
de La Rosa I. G., La Barbera F., Ferreras I., de Carvalho R. R., 2011, MNRAS, 418, L74
Fanelli M. N., O'Connell R. W., Burstein D., Wu C.-C., 1990, ApJ, 364, 272
Galametz A. et al., 2013, ApJS, 206, 10
Gallazzi A., Charlot S., Brinchmann J., White S. D. M., Tremonti C. A., 2005, MNRAS, 362, 41
Gallazzi A., Charlot S., Brinchmann J., White S. D. M., 2006, MNRAS, 370, 1106
Gallazzi A., Bell E. F., Zibetti S., Brinchmann J., Kelson D. D., 2014, ApJ, 788, 72
Glazebrook K. et al., 2017, Nature, 544, 71
Goddard D. et al., 2017, MNRAS, 465, 688
Goldoni P., Royer F., François P., Horrobin M., Blanc G., Vernet J., Modigliani A., Larsen J., 2006, Proceedings of the SPIE, 6269, 62692K
Greggio L., Renzini A., 1990, ApJ, 364, 35
Guarnieri P. et al., 2019, MNRAS, 483, 3060
Huang S., Ho L. C., Peng C. Y., Li Z.-Y., Barth A. J., 2013, ApJ, 766, 47
Johansson J., Thomas D., Maraston C., 2010, MNRAS, 406, 165
Juarez Y., Maiolino R., Mujica R., Pedani M., Marinoni S., Nagao T., Marconi A., Oliva E., 2009, A&A, 494, L25
Jørgensen I., Chiboucas K., 2013, AJ, 145, 77
Jørgensen I., Chiboucas K., Toft S., Bergmann M., Zirm A., Schiavon R. P., Grützbauch R., 2014, AJ, 148, 117
Kriek M., van Dokkum P. G., Labbé I., Franx M., Illingworth G. D., Marchesini D., Quadri R. F., 2009, ApJ, 700, 221
Kriek M. et al., 2016, Nature, 540, 248
La Barbera F., Ferreras I., de Carvalho R. R., Bruzual G., Charlot S., Pasquali A., Merlin E., 2012, MNRAS, 426, 2300
Lawrence A. et al., 2007, MNRAS, 379, 1599
Le Cras C., Maraston C., Thomas D., York D. G., 2016, MNRAS, 461, 766
Lonoce I., Longhetti M., Saracco P., Gargiulo A., Tamburri S., 2014, MNRAS, 444, 2048
Lonoce I. et al., 2015, MNRAS, 454, 3912
McCracken H. J. et al., 2010, ApJ, 708, 202
Madau P., Dickinson M., 2014, ARA&A, 52, 415
Mannucci F. et al., 2009, MNRAS, 398, 1915
Maraston C., 2005, MNRAS, 362, 799
Maraston C., Strömbäck G., 2011, MNRAS, 418, 2785
Maraston C., Thomas D., 2000, ApJ, 541, 126
Maraston C., Daddi E., Renzini A., Cimatti A., Dickinson M., Papovich C., Pasquali A., Pirzkal N., 2006, ApJ, 652, 85
Maraston C., Nieves Colmenárez L., Bender R., Thomas D., 2009, A&A, 493, 425
Maraston C., Pforr J., Renzini A., Daddi E., Dickinson M., Cimatti A., Tonini C., 2010, MNRAS, 407, 830
Maraston C. et al., 2013, MNRAS, 435, 2764
Martín-Navarro I., La Barbera F., Vazdekis A., Ferré-Mateu A., Trujillo I., Beasley M. A., 2015, MNRAS, 451, 1081
Martín-Navarro I., Vazdekis A., Falcón-Barroso J., La Barbera F., Yıldırım A., van de Ven G., 2018, MNRAS, 475, 3700
Mendel J. T. et al., 2015, ApJ, 804, L4
Moresco M., Jimenez R., Verde L., Cimatti A., Pozzetti L., Maraston C., Thomas D., 2016, J. Cosmol. Astropart. Phys., 12, 039
Naab T., Johansson P. H., Ostriker J. P., 2009, ApJ, 699, L178
Onodera M. et al., 2012, ApJ, 755, 26
Parikh T. et al., 2019, MNRAS, 483, 3420
Peebles P. J. E., 2002, 283, 351
Pforr J., Maraston C., Tonini C., 2012, MNRAS, 422, 3285
Pipino A., Matteucci F., 2004, MNRAS, 347, 968

Prevot M. L., Lequeux J., Maurice E., Prevot L., Rocca-Volmerange B., 1984, A&A, 132, 389

Sánchez-Blázquez P. et al., 2006, MNRAS, 371, 703

Santini P. et al., 2019, MNRAS, 486, 560

Segers M. C., Schaye J., Bower R. G., Crain R. A., Schaller M., Theuns T., 2016, MNRAS, 461, L102

Spolaor M., Forbes D. A., Proctor R. N., Hau G. K. T., Brough S., 2008, MNRAS, 385, 675

Spolaor M., Kobayashi C., Forbes D. A., Couch W. J., Hau G. K. T., 2010, MNRAS, 408, 272

Szomoru D. et al., 2010, ApJ, 714, L244

Thomas D., Kauffmann G., 1999, in Hubeny I., Heap S., Cornett R., eds, ASP Conf. Ser. Vol. 192, Spectrophotometric Dating of Stars and Galaxies. Astron. Soc. Pac., San Francisco, p. 261

Thomas D., Maraston C., Bender R., Mendes de Oliveira C., 2005, ApJ, 621, 673

Thomas D., Maraston C., Schawinski K., Sarzi M., Silk J., 2010, MNRAS, 404, 1775

Thomas D., Maraston C., Johansson J., 2011, MNRAS, 412, 2183

Thomas D. et al., 2013, MNRAS, 431, 1383

Toft S., Gallazzi A., Zirm A., Wold M., Zibetti S., Grillo C., Man A., 2012, ApJ, 754, 3

Trager S. C., Somerville R. S., 2009, MNRAS, 395, 608

Trager S. C., Faber S. M., Worthey G., González J. J., 2000a, AJ, 119, 1645

Trager S. C., Faber S. M., Worthey G., González J. J., 2000b, AJ, 120, 165

Trinchieri G., di Serego Alighieri S., 1991, AJ, 101, 1647

Trujillo I., Cenarro A. J., de Lorenzo-Cáceres A., Vazdekis A., de la Rosa I. G., Cava A., 2009, ApJ, 692, L118

van de Sande J. et al., 2011, ApJ, 736, L9

van de Sande J. et al., 2013, ApJ, 771, 85

Wilkinson D. M., Maraston C., Goddard D., Thomas D., Parikh T., 2017, MNRAS, 472, 4297

Williams C. C. et al., 2014, ApJ, 780, 1

Williams R. J., Quadri R. F., Franx M., van Dokkum P., Labbé I., 2009, ApJ, 691, 1879

Worthey G., 1994, ApJS, 95, 107

Worthey G., Ottaviani D. L., 1997, ApJS, 111, 377

Worthey G., Faber S. M., Gonzalez J. J., Burstein D., 1994, ApJS, 94, 687

Yan R., Newman J. A., Faber S. M., Konidaris N., Koo D., Davis M., 2006, ApJ, 648, 281

Yi S. K., Yoon S.-J., 2004, Ap&SS, 291, 205

Ziegler B. L., Thomas D., Böhm A., Bender R., Fritz A., Maraston C., 2005, A&A, 433, 519

## APPENDIX A: ANALYSIS ON MOCK SPECTRA

In this section, we discuss the derivation of stellar population parameters using different sets of spectral indices, in order to secure ourselves on the robustness of the results. Recall that – due to the variable data quality and different redshifts of the data – we were forced to use different combinations of indices in our analysis.

We constructed mock spectra having the same spectral characteristics of our data. We used stellar population models from MS11, with similar (known) stellar parameters as those obtained for our real galaxies. We downgraded the models to the velocity dispersion of each object and added a Gaussian random noise whose standard deviation is derived from the real S/N values in different spectral regions. Systematic errors are considered well below the statistical ones, so they were neglected. We repeated the addition of noise 1000 times in order to obtain a statistical sample of measured indices to be compared to models in the same way as we did for the real data.

As a first test, we compared the 1000 index realizations with the MS11–TMJ merged models (see Section 3.2) and retrieved ages and metallicities. We then selected the best-fitting solutions from the $\chi^2$ values. This procedure of parameter derivation was repeated for each mock using different sets of indices as it follows:

(i) All indices listed in Table 3.
(ii) The set of indices actually used for the given galaxy.
(iii) The sets of indices used for the other three objects.
(iv) Only UV indices, i.e. all the non-Lick indices located below 4000 Å, plus the D4000 break.
(v) Only Lick indices plus D4000.

The results are shown in Figs A1 and A2.

Differences among parameters obtained using different index subsets are negligible in all tests. The tests demonstrate that age and metallicity are retrieved with uncertainties similar to those obtained using real data, demonstrating that our analysis can be performed also on these low-S/N spectra.

Regarding the comparison between UV and Lick indices (Fig. A2), it is interesting to note that age distributions generally peak at younger ages for the UV indices and at older ages for the Lick indices, such that the combination of them is centred at the true value. This test demonstrates the value of adding the UV indices to the analysis of stellar populations.

For the second test, we included in the analysis also the information on [α/Fe] exploiting subsets of Lick indices in comparison with TMJ models as done in the real analysis. In this case, we constructed the mocks by perturbing 1000 times the values of the TMJ models assuming the error bars found from the previous tests. We choose to test a supersolar value of [α/Fe]=0.3 for all the four mock spectra. The set of Lick indices used in each fit is those used for the real data and given in Table 5.

The results are shown in Fig. A3. True values of age (left-hand panels), metallicity (middle panels), and [α/Fe] (right-hand panel) are shown with vertical dashed lines in each panel. To better visualize the uncertainties on the derived [α/Fe], the right-hand panels include a Gaussian fit to the histogram (red line) and its correspondent $\sigma$ value. From Fig. A3, it can be noticed that only in case of the simulated 7447 object the [α/Fe] value could not be constrained, exactly as we found when dealing with the real spectrum. This is expected since the available indices only include the Balmer lines of Hydrogen, which are mostly age sensitive (Worthey 1994).

These simulations demonstrate the feasibility of our analysis and ensure the results are robust.
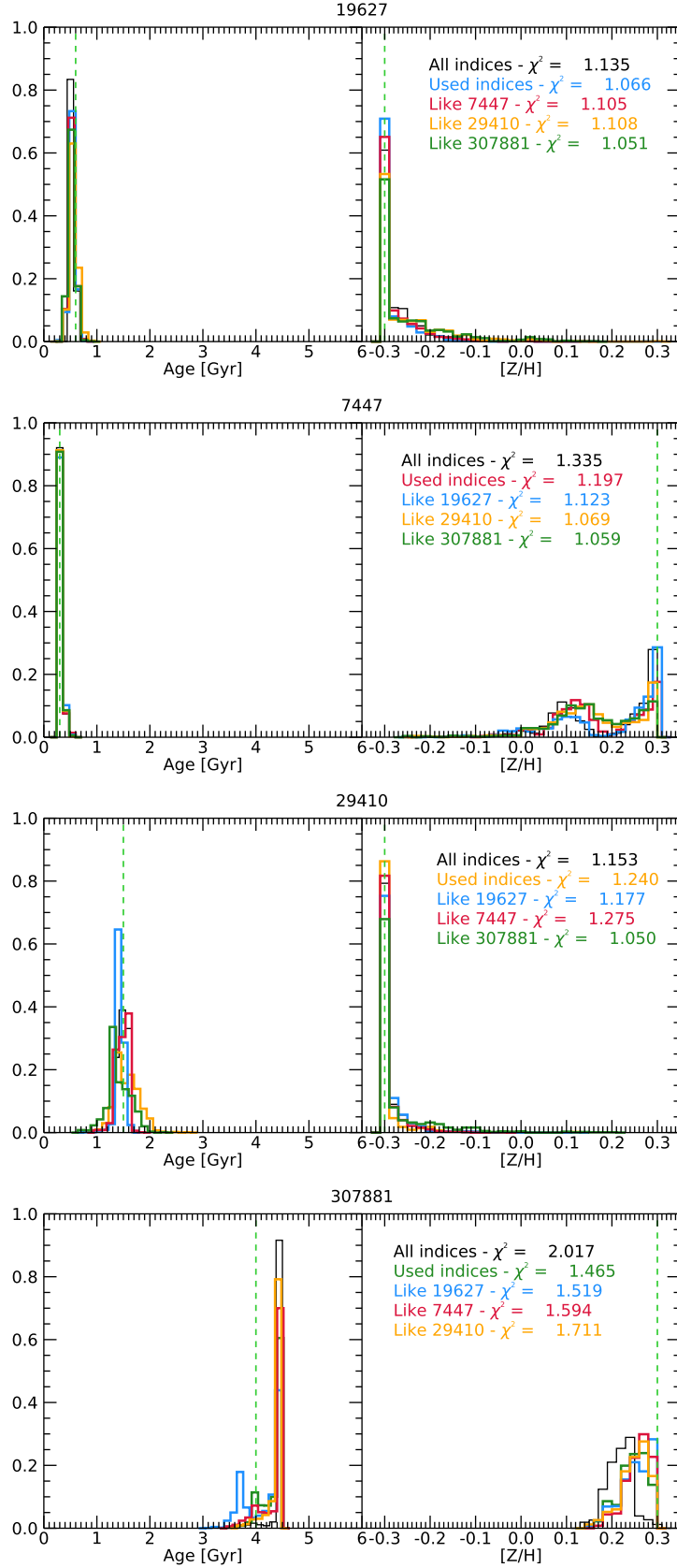
**Figure A1.** Mock spectra analysis: best-fitting age and metallicity distributions for different sets of indices. Mocks correspondent to the different galaxies are colour coded as: 19627: blue, 7447: red, 29410: orange, and 307881: green. All index distributions are shown in black. The vertical dashed green lines indicate the true input age and metallicity values. Reduced $\chi^2$s for each index set are also displayed.
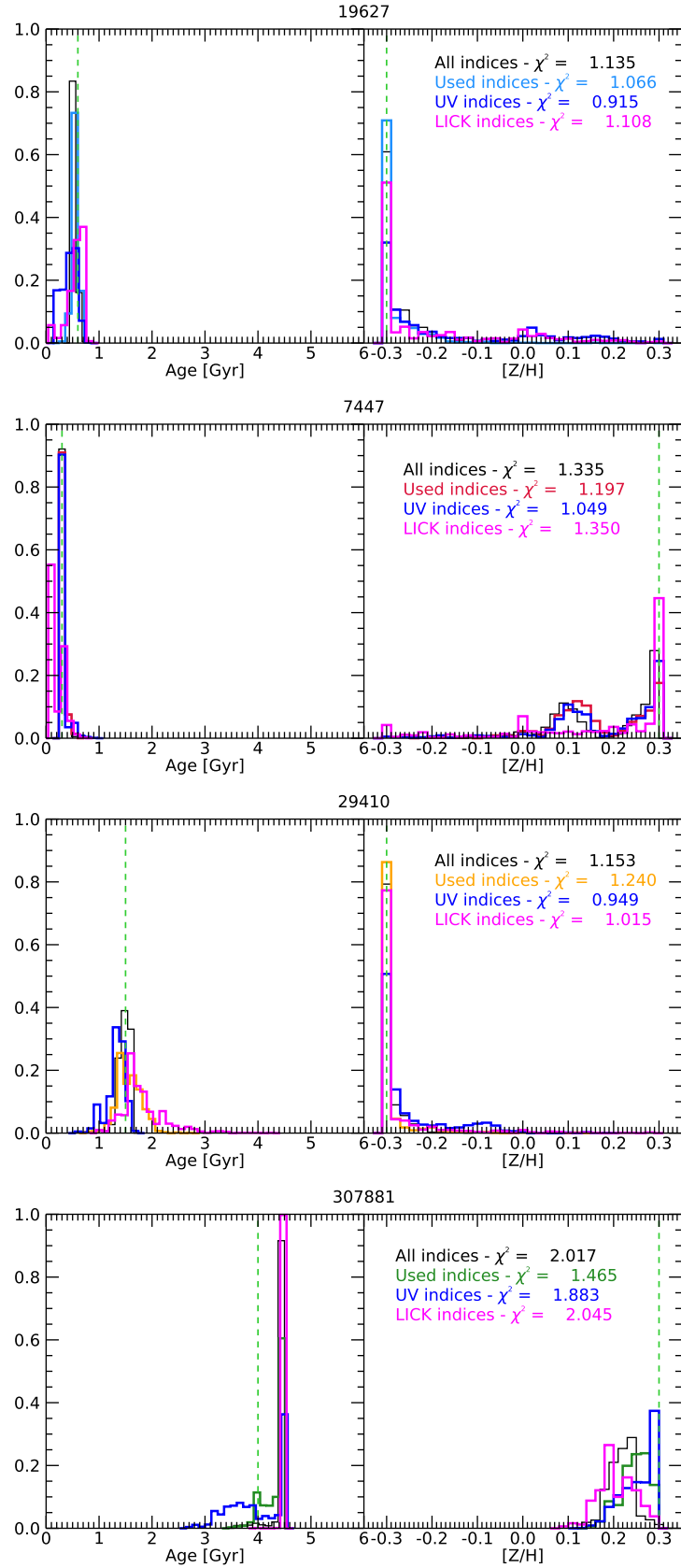
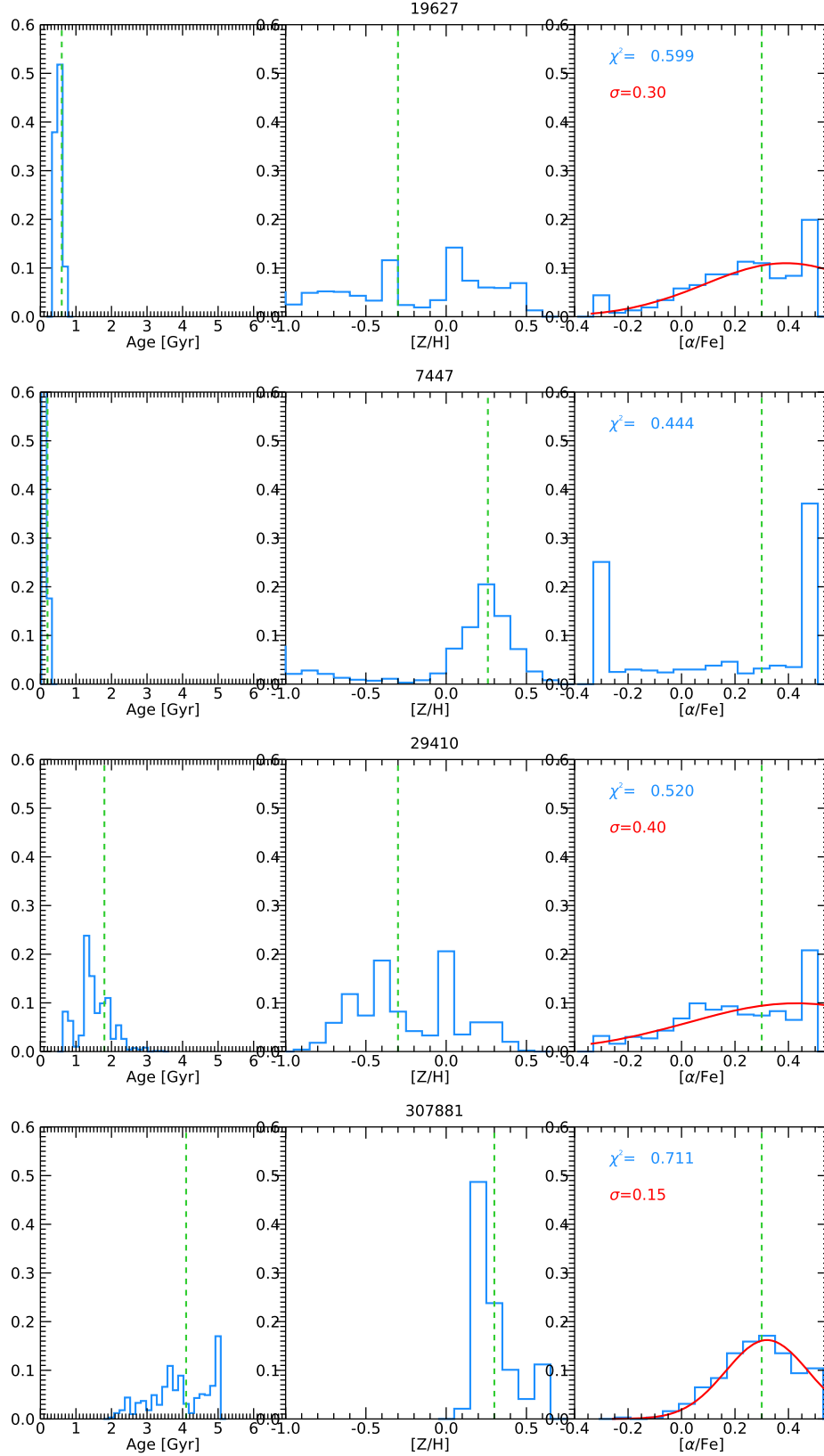**Figure A2.** As in Fig. A1, but now considering UV indices (blue lines) and Lick indices (magenta).

**Figure A3.** Mock spectra analysis: best-fitting age, metallicity, and [α/Fe] distributions for different sets of Lick indices as used for real data analysis (see Table 5). The vertical dashed green lines indicate the true input parameters values. A Gaussian fit to the [α/Fe] distribution is shown in red.

## APPENDIX B: COMPARISONS OF DATA AND BEST FITS FOR INDICES

Figs B1 and B2 show the comparison of the measured indices for the four galaxies with the correspondent best-fitting models. In particular, Fig. B1 refers to fits obtained with the MS11–TMJ merged models (Table 4), while Fig. B2 refers to fits obtained only using the TMJ models of Lick indices (Table 5).
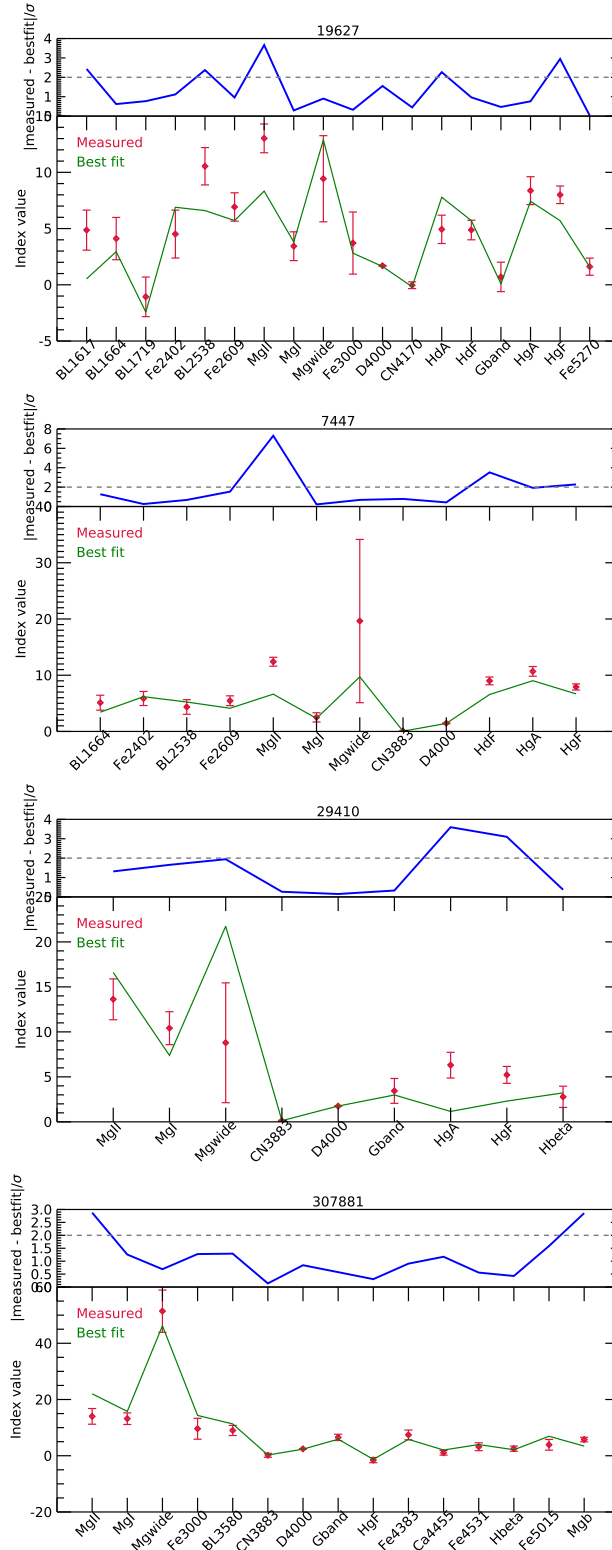
**Figure B1.** Comparison of best-fitting model indices (green line) with measured values (red diamonds) for each galaxy. MS11–TMJ best-fitting models are those reported in Table 4. Upper panels (blue line) show the differences between data and models divided by the measured error, indicating how many standard deviations they differ. The horizontal grey line indicates the $2\sigma$ level.

In each figure, the upper panel shows the values of the difference between data and best-fitting model divided by the measured error, suggesting how many standard deviations data and model differ. It can be seen that generally most of the best-fitting values agree with the data within $2\sigma$.
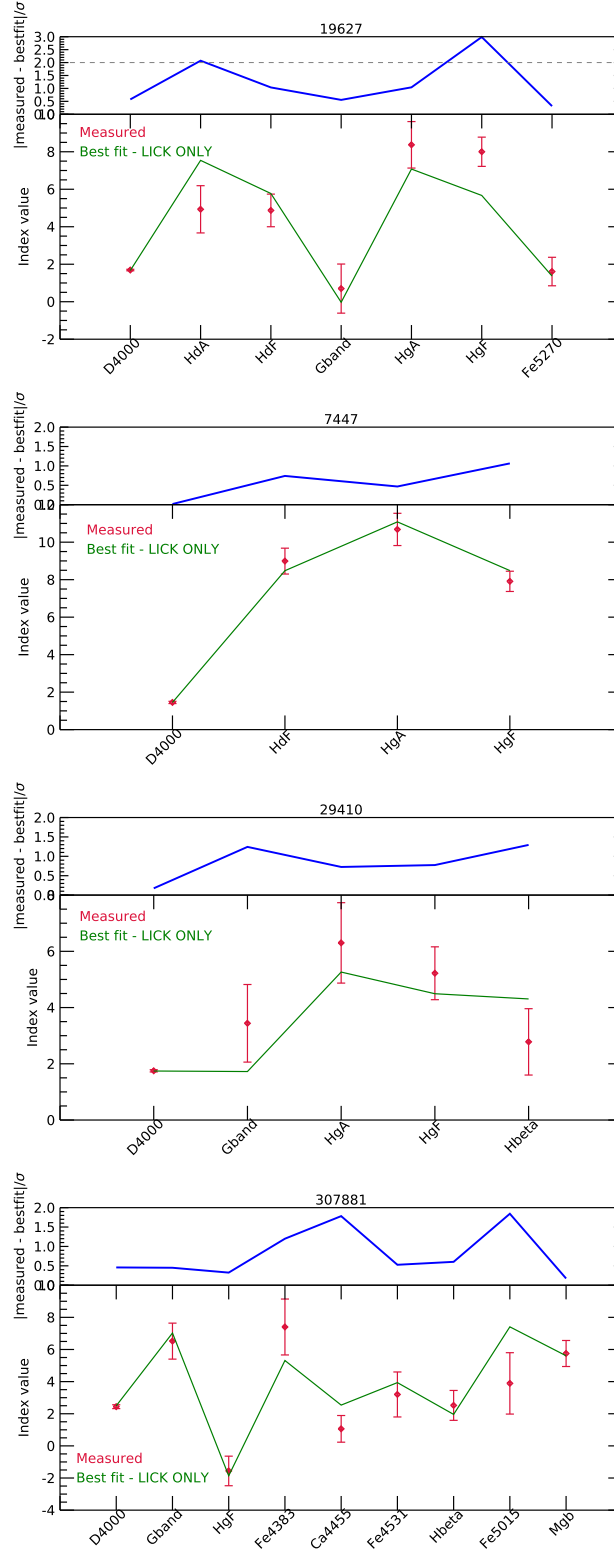


**Figure B2.** As in Fig. B1 for the TMJ best-fitting models reported in Table 5.

This paper has been typeset from a TEX/LATEX file prepared by the author.